Chapter 2
Voxel-Based Inversion Via Set-Theoretic Estimation

2.1 The Electromagnetic Model Equations

The starting point for any electromagnetic inverse problem is Maxwell's equations:

$$\begin{aligned}
\nabla \times \mathbf{E}(\mathbf{r}) &= -j\omega\mu_0 \mathbf{H}(\mathbf{r}) \\
\nabla \times \mathbf{H}(\mathbf{r}) &= j\omega\epsilon_0 \mathbf{E} + \sigma(\mathbf{r})\mathbf{E}(\mathbf{r}) \\
&= j\omega\epsilon_0 \mathbf{E}(\mathbf{r}) + (\sigma_f(\mathbf{r}) - \sigma_h)\mathbf{E}(\mathbf{r}) + \sigma_h \mathbf{E}(\mathbf{r}) \\
&= j\omega\epsilon_0 \mathbf{E}(\mathbf{r}) + \sigma^{(a)}(\mathbf{r})\mathbf{E}(\mathbf{r}) + \sigma_h \mathbf{E}(\mathbf{r}) \ , \qquad (2.1)
\end{aligned}$$

where $\sigma_f(\mathbf{r})$ is the flaw conductivity, σ_h is the uniform host conductivity, and $\sigma^{(a)}(\mathbf{r})$ is the anomalous conductivity. The product, $\sigma^{(a)}(\mathbf{r})\mathbf{E}(\mathbf{r})$ defines the anomalous electric current density, $\mathbf{J}(\mathbf{r})$.

The formal solution of Maxwell's equations can be obtained by equating the total electric field, $\mathbf{E}(\mathbf{r}) = \mathbf{J}(\mathbf{r})/\sigma_a(\mathbf{r})$, to the sum of the incident field, that is produced by the current in the exciter coil, and the scattered field, that is due to the anomalous electric current:

$$\begin{aligned}
E_x^{(i)}(\mathbf{r}) &= \frac{J_x(\mathbf{r})}{\sigma_a(\mathbf{r})} - E_x^{(s)}(\mathbf{r})\,[\mathbf{J}] \\
E_y^{(i)}(\mathbf{r}) &= \frac{J_y(\mathbf{r})}{\sigma_a(\mathbf{r})} - E_y^{(s)}(\mathbf{r})\,[\mathbf{J}] \\
E_z^{(i)}(\mathbf{r}) &= \frac{J_z(\mathbf{r})}{\sigma_a(\mathbf{r})} - E_z^{(s)}(\mathbf{r})\,[\mathbf{J}] \ . \qquad (2.2)
\end{aligned}$$

H. A. Sabbagh et al., *Advanced Electromagnetic Models for Materials Characterization and Nondestructive Evaluation*, Scientific Computation,
https://doi.org/10.1007/978-3-030-67956-9_2

The second term on the right-hand side of each of the equations in (2.2) stands for a linear functional, whose kernel is a Green's function. In order to discretize the integral relations implied in (2.2) by means of the method of moments, we define a regular three-dimensional grid of cells, each of dimension $\delta x \times \delta y \times \delta z$, and expand the current vector on this grid as

$$\begin{aligned} J_x(\mathbf{r}) &= \sum_{KLM} J^{(x)}_{KLM} T^{(x)}_{KLM}(\mathbf{r}) \\ J_y(\mathbf{r}) &= \sum_{KLM} J^{(y)}_{KLM} T^{(y)}_{KLM}(\mathbf{r}) \\ J_z(\mathbf{r}) &= \sum_{KLM} J^{(z)}_{KLM} T^{(z)}_{KLM}(\mathbf{r}) \, . \end{aligned} \tag{2.3}$$

The expressions for the $T^{(q)}_{klm}(\mathbf{r})$ are:

$$\begin{aligned} T^{(x)}_{klm}(\mathbf{r}) &= \pi_{2k}(x/\delta x)\pi_{1l}(y/\delta y)\pi_{1m}(z/\delta z) \\ T^{(y)}_{klm}(\mathbf{r}) &= \pi_{1k}(x/\delta x)\pi_{2l}(y/\delta y)\pi_{1m}(z/\delta z) \\ T^{(z)}_{klm}(\mathbf{r}) &= \pi_{1k}(x/\delta x)\pi_{1l}(y/\delta y)\pi_{2m}(z/\delta z) \, , \end{aligned} \tag{2.4}$$

where $\pi_{1m}(y/\delta y)$ is the mth unit pulse function, and $\pi_{2k}(x/\delta x)$ is the kth tent function, which is the convolution of $\pi_{1k}(x/\delta x)$ with itself (see Fig. 2.1).

The present version of **VIC-3D®** uses the Galerkin variant of the method of moments, in which testing is done with the same basis set that is used to expand the unknown currents. This differs from the earlier version, which used point-matching to complete the discretization. The implication for the present inverse problem is that we can no longer assume that the electric fields are known at the center of each cell; rather, we are given the moments of the electric field throughout each cell, as well as the expansion coefficients for the currents. We will now show how this knowledge can be used to determine the conductivity of each cell, if the anomalous currents are given.

The field moments for the x and y components of the (total) electric field are

$$E^x_{klm} = \int\int\int E^x(x,y,z) T^x_{klm}(x,y,z)\,dx\,dy\,dz \tag{2.5}$$

$$E^y_{klm} = \int\int\int E^y(x,y,z) T^y_{klm}(x,y,z)\,dx\,dy\,dz \, . \tag{2.6}$$

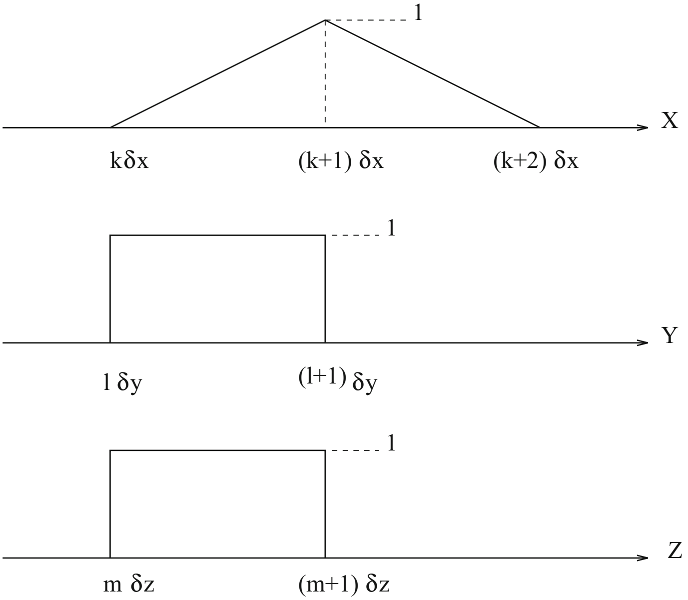

Fig. 2.1 Showing the location of the tent and pulse functions for the element $T^{(x)}_{klm}(x, y, z) = \pi_{2k}(x/\delta x)\pi_{1l}(y/\delta y)\pi_{1m}(z/\delta z)$

We can compute these from the discretized form of the volume-integral equations

$$\begin{aligned} E^x_{klm} &= E^{(i)(x)}_{klm} + \sum_{KLM} G^{(xx)}_{klm,KLM} J^x_{KLM} + \sum_{KLM} G^{(xy)}_{klm,KLM} J^y_{KLM} \\ &\quad + \sum_{KLM} G^{(xz)}_{klm,KLM} J^z_{KLM} \\ E^y_{klm} &= E^{(i)(y)}_{klm} + \sum_{KLM} G^{(yx)}_{klm,KLM} J^x_{KLM} + \sum_{KLM} G^{(yy)}_{klm,KLM} J^y_{KLM} \\ &\quad + \sum_{KLM} G^{(yz)}_{klm,KLM} J^z_{KLM} \, , \end{aligned} \tag{2.7}$$

where $E^{(i)}_{klm}$ are the field moments of the incident field, and the J_{KLM}'s are the expansion coefficients of the anomalous electric currents. The $G_{klm,KLM}$'s are the matrices that result from the discretization of the functionals with the Green's function kernels, and, thus, do not depend upon the cell conductivities.

We relate the cell conductivities to the electric field moments in the following way:

$$\mathbf{E} = \frac{\mathbf{J}^{(a)}(x, y, z)}{\sigma^{(a)}(x, y, z)} , \tag{2.8}$$

where $\mathbf{E}(x, y, z)$ is the total electric field, $\mathbf{J}^{(a)}(x, y, z)$ is the anomalous electric current, and $\sigma^{(a)}$ is the anomalous flaw conductivity. Upon substituting (2.8) into (2.5) and (2.6), we get

$$E^x_{klm} = \int\int\int \frac{J^{(a)(x)}(x, y, z)}{\sigma^{(a)}(x, y, z)} T^x_{klm}(x, y, z) dxdydz \tag{2.9}$$

$$E^y_{klm} = \int\int\int \frac{J^{(a)(y)}(x, y, z)}{\sigma^{(a)}(x, y, z)} T^y_{klm}(x, y, z) dxdydz . \tag{2.10}$$

Expanding $\mathbf{J}^{(a)}(x, y, z)$ in terms of the basis functions $T^x_{KLM}(x, y, z)$ and $T^y_{KLM}(x, y, z)$ gives

$$E^x_{klm} = \int\int\int \frac{\sum_{KLM} J^x_{KLM} T^x_{KLM}(x, y, z)}{\sigma^{(a)}(x, y, z)} T^x_{klm}(x, y, z) dxdydz \tag{2.11}$$

$$E^y_{klm} = \int\int\int \frac{\sum_{KLM} J^y_{KLM} T^y_{KLM}(x, y, z)}{\sigma^{(a)}(x, y, z)} T^y_{klm}(x, y, z) dxdydz . \tag{2.12}$$

We need to rewrite T^x_{KLM}, T^y_{KLM}, T^x_{klm}, and T^y_{klm} in terms of functions whose support is a single flaw cell. Thus, we write

$$T^x_{klm}(x, y, z) = R^x_{klm}(x, y, z) + S^x_{k+1lm}(x, y, z) \tag{2.13}$$

$$T^y_{klm}(x, y, z) = R^y_{klm}(x, y, z) + S^y_{kl+1m}(x, y, z) , \tag{2.14}$$

with the definitions

$$R^x_{klm}(x, y, z) = \begin{cases} \dfrac{x - k\delta x}{\delta x} & \text{for } k\delta x \le x \le (k+1)\delta x, \\ & \quad l\delta y \le y \le (l+1)\delta y,\ m\delta z \le z \le (m+1)\delta z \\ 0 & \text{otherwise} \end{cases} \tag{2.15}$$

$$S^x_{klm}(x, y, z) = \begin{cases} \dfrac{(k+1)\delta x - x}{\delta x} & \text{for } k\delta x \le x \le (k+1)\delta x, \\ & \quad l\delta y \le y \le (l+1)\delta y,\ m\delta z \le z \le (m+1)\delta z \\ 0 & \text{otherwise} \end{cases} \tag{2.16}$$

$$R^y_{klm}(x,y,z)=\begin{cases}\dfrac{y-l\delta y}{\delta y} & \text{for } k\delta x\le x\le (k+1)\delta x,\\ & \quad l\delta y\le y\le (l+1)\delta y,\ m\delta z\le z\le (m+1)\delta z\\ 0 & \text{otherwise}\end{cases}\tag{2.17}$$

$$S^y_{klm}(x,y,z)=\begin{cases}\dfrac{(l+1)\delta y-y}{\delta y} & \text{for } k\delta x\le x\le (k+1)\delta x,\\ & \quad l\delta y\le y\le (l+1)\delta y,\ m\delta z\le z\le (m+1)\delta z\\ 0 & \text{otherwise .}\end{cases}\tag{2.18}$$

Rewriting (2.11) and (2.12) in terms of these new functions gives

$$\begin{aligned}E^x_{klm}&=\iiint\sum_{KLM}J^x_{KLM}\left[\frac{R^x_{KLM}(x,y,z)}{\sigma_{KLM}}+\frac{S^x_{K+1LM}(x,y,z)}{\sigma_{K+1LM}}\right]\\&\qquad\left[R^x_{klm}(x,y,z)+S^x_{k+1lm}(x,y,z)\right]dxdydz\\ E^y_{klm}&=\iiint\sum_{KLM}J^y_{KLM}\left[\frac{R^y_{KLM}(x,y,z)}{\sigma_{KLM}}+\frac{S^y_{KL+1M}(x,y,z)}{\sigma_{KL+1M}}\right]\\&\qquad\left[R^y_{klm}(x,y,z)+S^y_{kl+1m}(x,y,z)\right]dxdydz\ ,\end{aligned}\tag{2.19}$$

where σ_{KLM} is the (uniform) conductivity of flaw cell KLM.

Because of the compact support of the basis functions, we have

$$\int\int\int R^x_{KLM}(x,y,z)R^x_{klm}(x,y,z)dxdydz=\frac{1}{3}\delta x\delta y\delta z\delta_{kK}\delta_{lL}\delta_{mM}\tag{2.20}$$

$$\int\int\int R^x_{KLM}(x,y,z)S^x_{klm}(x,y,z)dxdydz=\frac{1}{6}\delta x\delta y\delta z\delta_{kK}\delta_{lL}\delta_{mM}\tag{2.21}$$

$$\int\int\int R^y_{KLM}(x,y,z)R^y_{klm}(x,y,z)dxdydz=\frac{1}{3}\delta x\delta y\delta z\delta_{kK}\delta_{lL}\delta_{mM}\tag{2.22}$$

$$\int\int\int R^y_{KLM}(x,y,z)S^y_{klm}(x,y,z)dxdydz=\frac{1}{6}\delta x\delta y\delta z\delta_{kK}\delta_{lL}\delta_{mM}\ .\tag{2.23}$$

Putting these results into (2.19) gives

$$E^x_{klm}=\left(\frac{1}{3}\frac{J^x_{klm}}{\sigma_{klm}}+\frac{1}{6}\frac{J^x_{k+1lm}}{\sigma_{k+1lm}}+\frac{1}{6}\frac{J^x_{k-1lm}}{\sigma_{klm}}+\frac{1}{3}\frac{J^x_{klm}}{\sigma_{k+1lm}}\right)\delta x\delta y\delta z\tag{2.24}$$

$$E^y_{klm} = \left(\frac{1}{3}\frac{J^y_{klm}}{\sigma_{klm}} + \frac{1}{6}\frac{J^y_{kl+1m}}{\sigma_{kl+1m}} + \frac{1}{6}\frac{J^y_{kl-1m}}{\sigma_{klm}} + \frac{1}{3}\frac{J^y_{klm}}{\sigma_{kl+1m}} \right) \delta x \delta y \delta z \,. \quad (2.25)$$

By adding the following equations for E^x_{kl+1m} and E^y_{k+1lm},

$$E^x_{kl+1m} = \left(\frac{1}{3}\frac{J^x_{kl+1m}}{\sigma_{kl+1m}} + \frac{1}{6}\frac{J^x_{k+1l+1m}}{\sigma_{k+1l+1m}} + \frac{1}{6}\frac{J^x_{k-1l+1m}}{\sigma_{kl+1m}} + \frac{1}{3}\frac{J^x_{kl+1m}}{\sigma_{k+1l+1m}} \right) \delta x \delta y \delta z \quad (2.26)$$

$$E^y_{k+1lm} = \left(\frac{1}{3}\frac{J^y_{k+1lm}}{\sigma_{k+1lm}} + \frac{1}{6}\frac{J^y_{k+1l+1m}}{\sigma_{k+1l+1m}} + \frac{1}{6}\frac{J^y_{k+1l-1m}}{\sigma_{k+1lm}} + \frac{1}{3}\frac{J^y_{k+1lm}}{\sigma_{k+1l+1m}} \right) \delta x \delta y \delta z \quad (2.27)$$

we obtain four equations in the four unknowns, σ_{klm}, σ_{k+1lm}, σ_{kl+1m}, $\sigma_{k+1l+1m}$. These equations can be written in matrix form as:

$$\begin{bmatrix} x_{00} & x_{10} & 0 & 0 \\ y_{00} & 0 & y_{01} & 0 \\ 0 & 0 & x_{01} & x_{11} \\ 0 & y_{10} & 0 & y_{11} \end{bmatrix} \begin{bmatrix} \rho_{klm} \\ \rho_{k+1lm} \\ \rho_{kl+1m} \\ \rho_{k+1l+1m} \end{bmatrix} \delta x \delta y \delta z = \begin{bmatrix} E^x_{klm} \\ E^y_{klm} \\ E^x_{kl+1m} \\ E^y_{k+1lm} \end{bmatrix} , \quad (2.28)$$

where $\rho_{klm} = 1/\sigma_{klm}$ and

$$x_{00} = \frac{J^x_{klm}}{3} + \frac{J^x_{k-1lm}}{6} \,, \; y_{00} = \frac{J^y_{klm}}{3} + \frac{J^y_{kl-1m}}{6} \quad (2.29)$$

$$x_{10} = \frac{J^x_{klm}}{3} + \frac{J^x_{k+1lm}}{6} \,, \; y_{01} = \frac{J^y_{klm}}{3} + \frac{J^y_{kl+1m}}{6} \quad (2.30)$$

$$x_{01} = \frac{J^x_{kl+1m}}{3} + \frac{J^x_{k-1l+1m}}{6} \,, \; y_{10} = \frac{J^y_{k+1lm}}{3} + \frac{J^y_{k+1l-1m}}{6} \quad (2.31)$$

$$x_{11} = \frac{J^x_{kl+1m}}{3} + \frac{J^x_{k+1l+1m}}{6} \,, \; y_{11} = \frac{J^y_{k+1lm}}{3} + \frac{J^y_{k+1l+1m}}{6} \,. \quad (2.32)$$

Note that on the borders of the flaw, some of the expansion coefficients for the anomalous currents vanish. In particular

$$J^x_{klm} = \begin{cases} \text{nonzero} & 0 \le k \le N_x - 2, \; 0 \le l \le N_y - 1, \; 0 \le m \le N_z - 1 \\ \text{zero} & \text{otherwise} \end{cases} \quad (2.33)$$

$$J^y_{klm} = \begin{cases} \text{nonzero} & 0 \le k \le N_x - 1, \; 0 \le l \le N_y - 2, \; 0 \le m \le N_z - 1 \\ \text{zero} & \text{otherwise} \end{cases} \quad (2.34)$$

Inverting matrix equation (2.28) gives

$$\delta x \delta y \delta z \begin{bmatrix} \rho_{klm} \\ \rho_{k+1lm} \\ \rho_{kl+1m} \\ \rho_{k+1l+1m} \end{bmatrix} = \begin{bmatrix} \frac{x_{11}y_{01}y_{10}}{D} & \frac{-y_{11}x_{01}x_{10}}{D} & \frac{y_{01}y_{11}x_{10}}{D} & \frac{-y_{01}x_{11}x_{10}}{D} \\ \frac{-y_{00}y_{11}x_{01}}{D} & \frac{y_{11}x_{01}x_{00}}{D} & \frac{-y_{01}y_{11}x_{00}}{D} & \frac{x_{00}x_{11}y_{01}}{D} \\ \frac{-x_{11}y_{00}y_{10}}{D} & \frac{x_{00}x_{11}y_{10}}{D} & \frac{-y_{00}y_{11}x_{10}}{D} & \frac{y_{00}x_{11}x_{10}}{D} \\ \frac{x_{01}y_{00}y_{10}}{D} & \frac{-x_{00}x_{01}y_{10}}{D} & \frac{x_{00}y_{01}y_{10}}{D} & \frac{-y_{00}x_{01}x_{10}}{D} \end{bmatrix} \begin{bmatrix} E^x_{klm} \\ E^y_{klm} \\ E^x_{kl+1m} \\ E^y_{k+1lm} \end{bmatrix}, \tag{2.35}$$

where $D = x_{00}x_{11}y_{01}y_{10} - y_{00}y_{11}x_{01}x_{10}$. The solution for the σ's is

$$\begin{aligned} \sigma_{klm} &= \frac{(x_{00}x_{11}y_{01}y_{10} - y_{00}y_{11}x_{01}x_{10})\,\delta x \delta y \delta z}{x_{11}y_{01}y_{10}E^x_{klm} - y_{11}x_{01}x_{10}E^y_{klm} + y_{01}y_{11}x_{10}E^x_{kl+1m} - y_{01}x_{11}x_{10}E^y_{k+1lm}} \\ \sigma_{k+1lm} &= \frac{(x_{00}x_{11}y_{01}y_{10} - y_{00}y_{11}x_{01}x_{10})\,\delta x \delta y \delta z}{-y_{00}x_{01}y_{11}E^x_{klm} + y_{11}x_{01}x_{00}E^y_{klm} - y_{01}y_{11}x_{00}E^x_{kl+1m} + y_{01}x_{11}x_{00}E^y_{k+1lm}} \\ \sigma_{kl+1m} &= \frac{(x_{00}x_{11}y_{01}y_{10} - y_{00}y_{11}x_{01}x_{10})\,\delta x \delta y \delta z}{-x_{11}y_{00}y_{10}E^x_{klm} + x_{11}x_{00}y_{10}E^y_{klm} - y_{00}y_{11}x_{10}E^x_{kl+1m} + y_{00}x_{11}x_{10}E^y_{k+1lm}} \\ \sigma_{k+1l+1m} &= \frac{(x_{00}x_{11}y_{01}y_{10} - y_{00}y_{11}x_{01}x_{10})\,\delta x \delta y \delta z}{x_{01}y_{00}y_{10}E^x_{klm} - y_{10}x_{01}x_{00}E^y_{klm} + y_{01}y_{10}x_{00}E^x_{kl+1m} - y_{00}x_{01}x_{10}E^y_{k+1lm}}. \end{aligned} \tag{2.36}$$

This solution for the σ's will not exist unless the system, (2.28), is independent. There are many situations that are likely to arise which will result in dependence among these equations, and we, therefore, turn to a different method of 'solving' (2.28), which we call the 'two-cell' hypothesis. Consider a 2 × 2 array of adjacent cells in the x- and y-directions. We call this array a 'window pane,' and ask for the solution of (2.28) under the hypothesis that two adjacent cells in the window pane have equal conductivities. The answer is:

$$\begin{aligned} \sigma_{klm} &= \sigma_{k+1lm} &&= \frac{(x_{00} + x_{10})}{E^x_{klm}} \\ \sigma_{klm} &= \sigma_{kl+1m} &&= \frac{(y_{00} + y_{01})}{E^y_{klm}} \\ \sigma_{kl+1m} &= \sigma_{k+1l+1m} &&= \frac{(x_{01} + x_{11})}{E^x_{kl+1m}} \\ \sigma_{k+1lm} &= \sigma_{k+1l+1m} &&= \frac{(y_{10} + y_{11})}{E^y_{k+1lm}} \end{aligned} \tag{2.37}$$

Of course, this results in non-unique solutions; each cell in the window pane has two solutions. In fact, because the σ's are known to be real, we can separate the x's and y's and E's into their real and imaginary parts, and get four solutions for each cell of the window pane. Each solution, then, is an outcome of an experiment, in the language of set-theoretic estimation theory, and is a candidate for processing by the robust statistical estimator that is described in the next chapter.

The integral relation that allows us to determine the anomalous current is derived from the measurement process. Typically, we measure the perturbation of the probe impedance, ΔZ, due to the flaw. Adopting the probe current $\mathbf{J}_p$ as the phase reference, this impedance is given by:

$$\begin{aligned} I^2 \Delta Z &= -\int_{coil} \mathbf{E}^{(s)}(\mathbf{r}) \cdot \mathbf{J}_p(\mathbf{r}) d\mathbf{r} \\ &= -\int_{flaw} \mathbf{E}^{(i)}(\mathbf{r}) \cdot \mathbf{J}(\mathbf{r}) d\mathbf{r}, \end{aligned} \tag{2.38}$$

where I is the total driving-current in the probe coil. In arriving at the final expression, we used a reciprocity theorem (see [111, Chapter 5]) that relates the scattered field, $\mathbf{E}^{(s)}$, at the primary source (the eddy-current probe coil) to the incident field at the secondary source (the anomalous current source due to the flaw).

The integral expression, (2.38), is discretized by substituting the expansions, (2.3), for the currents, and making use of the definitions of the field moments, (2.5), (2.6). The result is quickly obtained:

$$\Delta Z = -\sum_{KLM} \left(J^{(x)}_{KLM} E^{(i)(x)}_{KLM} + J^{(y)}_{KLM} E^{(i)(y)}_{KLM} \right) , \tag{2.39}$$

where we assume that $I = 1$, and that the exciting coils produce an incident field that is oriented in the (x, y)-plane; i.e., $E^{(i)(z)}_{KLM} = 0$.

2.2 Set-Theoretic Estimation

We quote Combettes [27, p. 202]

> The basic philosophical motivation for the set theoretic approach is that more reliable solutions can be obtained by exploiting known information rather than imposing an often subjective notion of optimality. Thus, in the set theoretic framework, the emphasis is placed on the feasibility of a solution rather than its optimality, as is done in the conventional approach. The goal is not to produce a "best" solution but one that is consistent with all available information. In set theoretic estimation, all the members of the feasibility set are acceptable solutions. They can be regarded as the objects that, in light of all available information, may have given rise to the observed data. The only way to restrict objectively the feasibility set is to incorporate more information in the formulation. If some of the feasible solutions are not acceptable, then it must be the case that the formulation fails to

> include some constraint that has not been identified. Once the set based on this constraint is incorporated, any point in the feasibility set should be acceptable; if not the cycle is repeated. Usually, there is more than one solution, which may be counterintuitive from the standpoint of conventional point estimation theory where, to extract a single solution, an objective function with a unique extremum is employed. On the other hand, because of the arbitrariness in the selection of such an objective function, the result is, at best, nothing but a qualitative selection of a feasible solution.

In set theoretic estimation, we do not seek a unique solution, as in optimization, but we seek the set of feasible solutions; all such solutions are acceptable [27]. A feasible solution is one that is consistent with all available information, such as the field equation, (2.41), and the data equation, (2.40), both shown below.

The algorithm that we are developing is based on statistical decision theory applied to the outcomes of a number of "experiments." Each experiment is labeled by the view-index v that is associated with the frequency of excitation and position of the exciting probe in the eddy-current NDE process. The outcomes of the experiments are elements of the "feasibility set," in the language of set theoretic estimation; that is, they satisfy all known information about the problem.

We write the data equation and the field equation as

$$Z(v) = -\sum_{LMJ} \mathbf{E}^{(i)}_{LMJ}(v) \cdot \mathbf{J}_{LMJ}(v) \tag{2.40}$$

$$\mathbf{E}^{(i)}_{lmj}(v) = \mathbf{E}_{lmj}(v) - \sum_{LMJ} G^{(ee)}_{jJ}(l-L, m-M; \omega) \cdot \mathbf{J}_{LMJ}(v) \ , \tag{2.41}$$

respectively, where $G^{(ee)}$ is an 'electric-electric' Green's dyadic, that transforms an electric current into an electric field moment.[1] Note that (2.40) and (2.41) are linear in all the variables.

We define the vth "experiment" to be the pair $(Z(v), \mathbf{E}^{(i)}_{lmj}(v))$, and the "outcomes" of this experiment to be the pair $(\mathbf{J}_{lmj}(v), \mathbf{E}_{lmj}(v))$, which satisfy (2.40) and (2.41). Thus, the outcomes are feasible because they satisfy all known information about the problem. Clearly, we cannot talk about a unique solution, because the feasible set contains many points.

In the problems that are described in this chapter, we model a single transmitting coil to excite the system, and a single receiver coil that is scanned over the region of interest. In place of a single, movable, receiver coil, it is possible to use a fixed array of receivers. In either case, this is an example of a transmit-receive (T/R) configuration, which is becoming more widely used in the NDE industry. The use of a T/R configuration allows us to gain more information from each experiment (i.e., from each viewing).

For example, if we have a single excitation source (the transmitter), and a single receiver sensor that is scanned over N_s points, then each view, v, produces N_s results, $\{Z_1(v), \ldots, \ Z_{N_s}(v)\}$. The actual current $\mathbf{J}_{LMJ}(v)$, however, is associated

---

[1] We consider only problems in which the host and anomalies are nonmagnetic.

only with the transmitter, because the transmitter is the sole exciter of the system (the receiver is assumed to carry no current). Hence, (2.40) is replaced by

$$\begin{aligned}
Z_1(v) &= -\sum_{LMJ} \mathbf{E}^{(1)}_{LMJ}(v) \cdot \mathbf{J}_{LMJ}(v) \\
Z_2(v) &= -\sum_{LMJ} \mathbf{E}^{(2)}_{LMJ}(v) \cdot \mathbf{J}_{LMJ}(v) \\
&\vdots \\
Z_{N_s}(v) &= -\sum_{LMJ} \mathbf{E}^{(N_s)}_{LMJ}(v) \cdot \mathbf{J}_{LMJ}(v) \,,
\end{aligned} \tag{2.42}$$

where $\mathbf{E}^{(n)}_{LMJ}(v)$ is the "incident" field produced by the sensor when it is in its nth scan position, during the vth view. This field is known a priori, because we know the location and geometry of the receiving sensor during the vth view.

The minimum-norm solution of (2.42) is given by

$$\widetilde{\mathbf{J}}_{LMJ}(v) = \mathscr{M}^{\dagger}(v) \begin{bmatrix} Z_1(v) \\ \vdots \\ Z_{N_s}(v) \end{bmatrix} , \tag{2.43}$$

where $\mathscr{M}^{\dagger}(v)$ is the pseudoinverse of the matrix in (2.42). In the examples of this chapter, we used the QR-decomposition [62] to compute the minimum-norm solution. The algorithm that is presented in [62] to solve for the minimum-norm solution allows the user to define a tolerance level, from which an effective pseudo-rank is obtained for the system matrix. The tolerance is chosen to produce a stable solution in the presence of noisy data.

The electric field produced by this current is gotten by substituting (2.43) into (2.41):

$$\widetilde{\mathbf{E}}_{lmj}(v) = \mathbf{E}^{(i)}_{lmj}(v) + \sum_{LMJ} G^{(ee)}_{jJ}(l-L, m-M; \omega) \cdot \widetilde{\mathbf{J}}_{LMJ}(v) \,. \tag{2.44}$$

Note that this is the correct electric field-moment corresponding to the current $\widetilde{\mathbf{J}}$, and **VIC-3D®** computes this field very quickly and accurately. This gives **VIC-3D®** the advantage over other field-solving methods, such as finite-elements or finite-differences. More important, however, is that (2.44) is the unique field-moment associated with the current, and is calculated to the same precision as the current, which will ensure that the final step in the algorithm, namely the statistical decision step that is described below, will be meaningful.

Given the electric field moments, we can then calculate an expansion for the electric field within the flaw. The resulting electric field expansion coefficients will be called $\widetilde{\mathbf{e}}_{lmj}$. Hence, for this value of the view-index, v, we associate the triple, $(\widetilde{J}_x, \widetilde{e}_x)_{lmj}(v)$, $(\widetilde{J}_y, \widetilde{e}_y)_{lmj}(v)$, $(\widetilde{J}_z, \widetilde{e}_z)_{lmj}(v)$, with the lmjth cell, and when we take the ratio of the electric current to the electric field at the middle of the lmjth cell, we arrive at the conductivity, σ_{lmj} of the lmjth cell, which is our final goal. We then perform another experiment by choosing another value of v, thereby generating another triplet. This ensemble of triplets constitutes the feasible set for each cell.

2.3 Statistical Analysis of the Feasible Set

One of the principal efforts of research in Set-Theoretic Estimation is to determine the number and nature of the experiments, $(Z(v), \mathbf{E}^{(i)}_{lmj}(v))$, and receiver scans, $\mathbf{E}^{(n)}_{LMJ}$, that produce a good feasible set for statistical analysis. As might be expected, this depends upon the complexity of the flaw that is to be reconstructed, and upon the resolution desired in the reconstruction.

After deducing the feasibility set, we are then faced with the task of assigning a single number for the conductivity of each cell; this is a problem of data analysis, which uses robust regression, as described in [111, Chapter 13]. The aim of the statistical analysis of the feasible set is to fit a constant through the data, which are produced by the algorithm described in the preceding section, for all views (or experiments), v.

A beneficial feature of this algorithm is that the analysis of the data set for each cell is done independently of every other cell; i.e., a decision is made on a cell-by-cell basis. Since the decision to be made for each cell involves a nonlinear (robust) estimator, the computational burden is greatly reduced when compared to using a nonlinear estimator to solve for many cells jointly. (The bilinear conjugate-gradient algorithm is an exception.) Furthermore, this leads us to a constrained iterative ('layer-stripping') algorithm, that uses the known and accepted results for some cells to determine the results for others at a later stage of the iteration.

2.4 A Layer-Stripping Algorithm

A classical layer-stripping algorithm consists of solving an inverse problem layer-by-layer, when the physical system permits such a reconstruction. If the excitation and detection methods permit only one layer to be detected, say due to timing arrangements in a pulsed system, then only that layer will be reconstructed. This reconstruction, then, constitutes known data for the reconstruction of the next layer.

In our situation, we have discovered that we can reconstruct certain cells accurately, similar to the reconstruction of a layer, and we then want to use this result in the reconstruction of the remaining cells. We do not assume that an entire layer has been reconstructed, nor that we will reconstruct on a layer-by-layer basis.

The proposed algorithm proceeds as follows: suppose that we have successfully reconstructed the conductivity of each cell of a 2 × 2 window pane. That means that we know $\sigma_{klm},\ \sigma_{k+1lm},\ \sigma_{kl+1m},\ \text{and}\sigma_{k+1l+1m}$; hence, all of the coefficients in (2.24) and (2.25) are well-defined. Then, we substitute these equations into the left-hand sides of the field equations, (2.7), and derive the constraint equations:

$$\left(\frac{1}{3}\frac{J^x_{klm}}{\sigma_{klm}}+\frac{1}{6}\frac{J^x_{k+1lm}}{\sigma_{k+1lm}}+\frac{1}{6}\frac{J^x_{k-1lm}}{\sigma_{klm}}+\frac{1}{3}\frac{J^x_{klm}}{\sigma_{k+1lm}}\right)\delta x\delta y\delta z =$$

$$E^{(i)(x)}_{klm}+\sum_{KLM}G^{(xx)}_{klm,KLM}J^x_{KLM}+\sum_{KLM}G^{(xy)}_{klm,KLM}J^y_{KLM}+\sum_{KLM}G^{(xz)}_{klm,KLM}J^z_{KLM}$$

$$\left(\frac{1}{3}\frac{J^y_{klm}}{\sigma_{klm}}+\frac{1}{6}\frac{J^y_{kl+1m}}{\sigma_{kl+1m}}+\frac{1}{6}\frac{J^y_{kl-1m}}{\sigma_{klm}}+\frac{1}{3}\frac{J^y_{klm}}{\sigma_{kl+1m}}\right)\delta x\delta y\delta z =$$

$$E^{(i)(y)}_{klm}+\sum_{KLM}G^{(yx)}_{klm,KLM}J^x_{KLM}+\sum_{KLM}G^{(yy)}_{klm,KLM}J^y_{KLM}$$

$$+\sum_{KLM}G^{(yz)}_{klm,KLM}J^z_{KLM}\ , \tag{2.45}$$

The unknowns in this equation are the currents in all the cells (including klm); everything else is known. This equation, which is of the form that **VIC-3D®** solves, constitutes a constraint on the system of data equations (2.42). Of course, we get an equation that is identical to (2.45) for each successfully reconstructed window-pane. The system of such equations is consistent, and generally well conditioned. Note, in particular, that if $\sigma_{klm}=0$ then the constraint equations become $J^x_{klm}=J^x_{k-1lm}=J^y_{klm}=J^y_{kl-1m}=0$.

Thus, our problem now is to determine a minimum-norm (least-squares) solution of (2.42), subject to the linear constraint(s) of (2.45). We appeal to well-known algorithms in linear least-squares problems. Lawson and Hanson [62, pp.134–157] give three algorithms, together with supporting code, to solve this problem. Each of the three methods consists of three stages:

1. Derive a lower-dimensional unconstrained least squares problem from the given problem.
2. Solve the derived problem.
3. Transform the solution of the derived problem to obtain the solution of the original constrained problem.

In Lawson and Hanson's first method, one makes use of an orthogonal basis for the null space of the matrix of the constraint equations. If the problem does not have a unique solution, this method will produce the unique minimum norm solution of the original constrained problem. Furthermore, this method has the very attractive feature of being amenable to numerically stable updating techniques, which will be necessary as we add more rows to the constraint equation; this will happen as we satisfactorily reconstruct more and more cells.

The second method uses direct elimination by premultiplication using both orthogonal and nonorthogonal transformation matrices, and the third solves the problem by using weighted least-squares. We have tested the second and third methods, and have found them to produce good results. We used the second method in the examples reported later in this chapter.

Once the minimum-norm solution of the constrained least-squares problem has been computed, the algorithm proceeds as before. The currents are substituted into (2.41), thereby determining the total field in each cell (we can exclude cell klm, unless we believe that it could be improved). Then the feasibility set is fitted with a straight line by means of robust estimation; the slope of this line is accepted as the normalized conductivity of the cell.

If we are still not satisfied with the results of one or more cells, we will perform a new experiment. The experiment could be simply a new frequency of excitation, which would make the process a multifrequency algorithm.

2.5 Some Examples of the Inversion Algorithm

Introduction The model examples in this section include surface-breaking and buried flaws in a half-space. We simulate a transmit-receive (T/R) probe configuration, which includes a single transmitting and receiving probe. Each probe is scanned independently of the other, but the receiving probe is assumed to be connected to an infinite-impedance amplifier. This means that it carries no current; hence, the excitation of the flaw is accomplished solely by means of the transmitter probe. In all cases the transmitting and receiving coils are identical.

In all the problems considered in this chapter, the host region is a half-space, whose conductivity is 10^5 S/m. The anomalous conductivity is normalized to have a value $\sigma_a = \sigma_f/\sigma_h - 1$, where σ_f is the conductivity of the flaw, and σ_h is the conductivity of the host. Hence, for a void, in which the conductivity of the flaw, $\sigma_f = 0$, we have $\sigma_a = -1$, and this is the smallest value that the anomalous conductivity can take, because $\sigma_f \geq 0$. For an unflawed cell, $\sigma_f = \sigma_h$, which implies that $\sigma_a = 0$.

In principle, there is no upper limit to the value that σ_a can assume, but in practice the conductivity of the flaw is not likely to exceed that of copper ($= 5.8 \times 10^7$), which means that for typical host materials, whose conductivities are in the range 10^6 to 10^7, σ_a is likely to be bounded by 9 or so. In the numerical experiments presented here, we used this as our upper bound in searching for the best fit for the conductivity of each cell.

A Surface-Breaking Slot at 50 kHz Consider a cubic region intersecting the surface of the half-space and extending 3 mm vertically (the z-direction) into the half-space. The (x, y) dimensions are also 3 mm, centered at the origin in (x, y)-

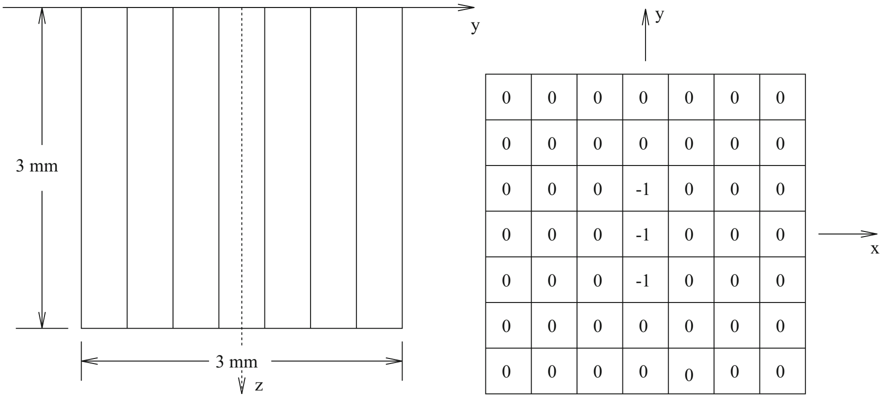

0	0	0	0	0	0	0
0	0	0	0	0	0	0
0	0	0	-1	0	0	0
0	0	0	-1	0	0	0
0	0	0	-1	0	0	0
0	0	0	0	0	0	0
0	0	0	0	0	0	0

Fig. 2.2 A surface-breaking slot. Those cells labeled '0' are unflawed, and those labeled '-1' are empty (zero conductivity)

space. This cube is partitioned into forty-nine cells in the (x, y)-plane, and one cell in the z-direction. The middle three cells are filled with air ($\sigma_a = -1$), and the remaining forty-six are filled with host material ($\sigma_a = 0$), as shown in Fig. 2.2. This arrangement constitutes a surface-breaking slot, whose precise location in the (x, y)-plane is uncertain. The frequency of excitation is 50 kHz, which produces a skin-depth of

$$\begin{aligned}\delta_s &= \sqrt{\frac{2}{2\pi f \mu \sigma_h}} \\ &= \sqrt{\frac{2}{2\pi \times 5 \times 10^4 \times 4\pi \times 10^{-7} \times 10^5}} \\ &= 7.12 \text{ mm} . \end{aligned} \tag{2.46}$$

The transmitting coil is scanned over the (x, y)-plane, using 16 equi-spaced points in each direction, starting at coordinates $(-3.0, -3.0)$ and ending at $(3.0, 3.0)$. This scan constitutes 256 'experiments.' The outcome of each of these experiments is obtained by scanning the receiver coil over the same (x, y)-raster as for the transmitter, when the transmitter is fixed at each of its points. This gives us 256 complex equations, with 98 complex unknowns (the x and y-components of the anomalous current in each cell), which are to be massaged by the QR-decomposition, producing a single least-squares estimate of the complex current in each cell. The algorithm then produces the x and y-components of the corresponding complex electric field within each cell; these are the feasibility sets that are defined above.

We display the feasibility sets for cells numbered 18, 25, and 32 in Fig. 2.3. Clearly, the data favor a conductivity value of -1, and that is what the LMS-

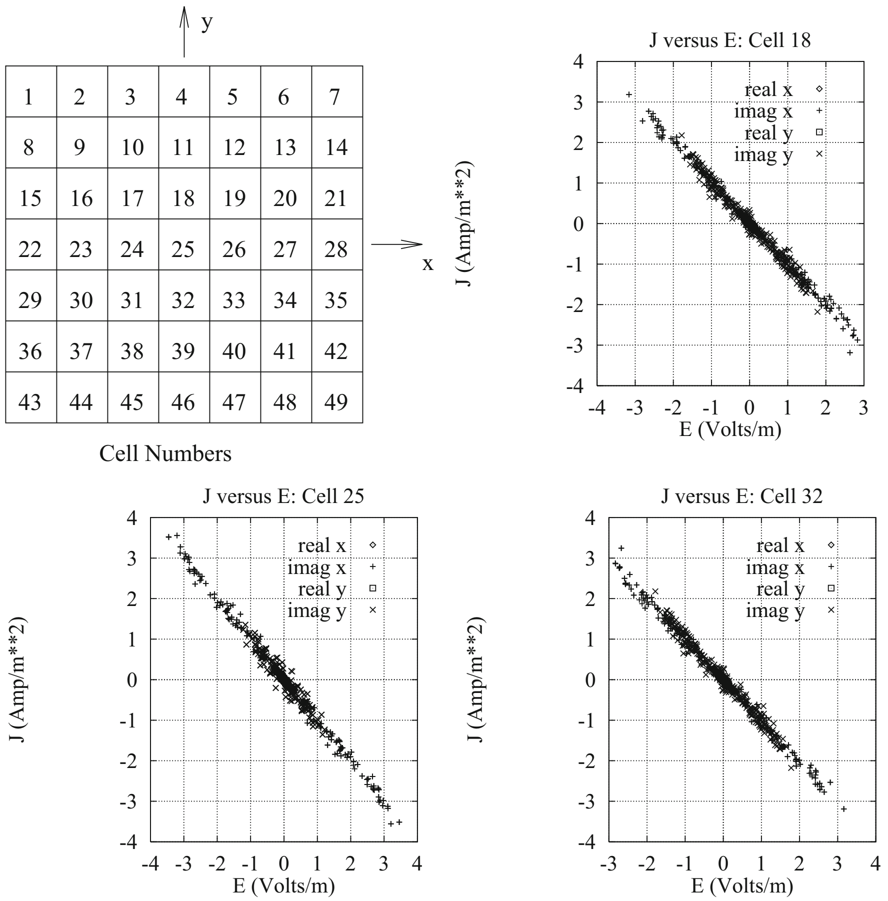

1	2	3	4	5	6	7
8	9	10	11	12	13	14
15	16	17	18	19	20	21
22	23	24	25	26	27	28
29	30	31	32	33	34	35
36	37	38	39	40	41	42
43	44	45	46	47	48	49

Fig. 2.3 Feasibility sets for cells numbered 18, 25, and 32

estimator produces in the reconstruction shown in Fig. 2.4. This, of course, is the exact answer for these three cells.

In Fig. 2.5 we show feasibility sets for cells numbered 1, 17, and 26. These cells are unflawed, but only cell number 1 is reconstructed exactly. Despite this fact, this reconstruction can be useful in practical NDE, because it indicates clearly the presence of a flaw, and gives a reasonable estimate of its size. An application of the S-estimator as well as the classical least-squares estimator produced essentially the same results.

We can get an idea of the quality of the reconstruction of each cell (or, to put it roughly, the confidence we can place on the results), by plotting the logarithm of the median of the squares of the residuals (if we are using the LMS-estimator) versus theta. The algorithm requires us to choose the minimum of this function, so we wish to determine the global picture to determine the ‘quality’ of this minimum. We show

Fig. 2.4 Reconstruction of the flaw of Fig. 2.2. The LMS-estimator was used for this reconstruction

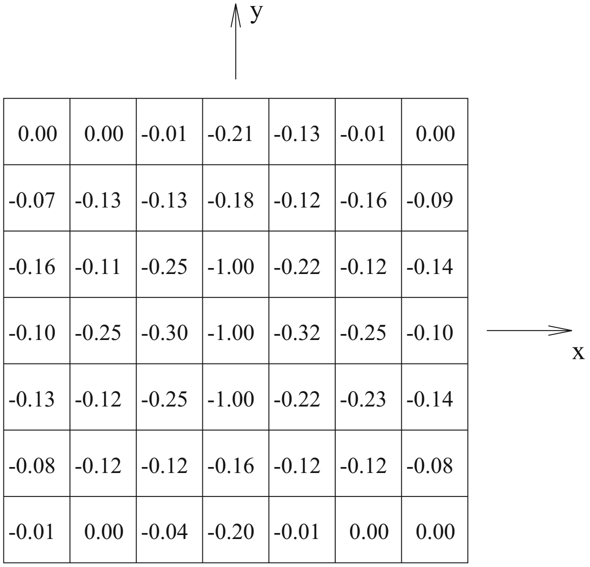

0.00	0.00	-0.01	-0.21	-0.13	-0.01	0.00
-0.07	-0.13	-0.13	-0.18	-0.12	-0.16	-0.09
-0.16	-0.11	-0.25	-1.00	-0.22	-0.12	-0.14
-0.10	-0.25	-0.30	-1.00	-0.32	-0.25	-0.10
-0.13	-0.12	-0.25	-1.00	-0.22	-0.23	-0.14
-0.08	-0.12	-0.12	-0.16	-0.12	-0.12	-0.08
-0.01	0.00	-0.04	-0.20	-0.01	0.00	0.00

these results in Fig. 2.6 for cells 18, 25, and 32, and in Fig. 2.7 for cells 1, 17, and 26.

We will use figures such as these in some of our other examples to explain the results of reconstructions.

Buried Void at 50 MHz We take the same slot configuration of the preceding example, except to make it only 1.5 mm deep, bury it under a host layer that is also 1.5 mm thick, and excite this system at 50 MHz. Our use of 50 MHz stems from our interest in improving the resolution of the reconstructions of the preceding example, and is guided by the following argument. The (x, y) cell dimensions are 0.429 mm, and the skin depth at 50 kHz is 7.12 mm. At 50 MHz, the skin depth is 0.225 mm, which is about one-half the cell dimensions. The skin effect is isotropic, which means that a localized source radiating in the host material will have its signal reduced to $1/e = 0.368$ in 0.225 mm, in any direction, at 50 MHz. Thus, at this frequency, we expect two nearby cells to be well distinguished as compared to the situation at 50 kHz. The use of the over-layer of host material is merely to make the problem more challenging and realistic. We used the same raster scan for both transmitter and receiver as in Section (a), but the inversion process now involves 98 cells, since we are attempting to reconstruct the top layer, as well as the buried void. That is, we are assuming that we know nothing about the depth of the void. The system is shown in Fig. 2.8; the upper grid corresponds to the 49 cells of the host layer, and the lower grid shows the flaw.

The results of the inversion support our conjecture about the smaller skin depth aiding the resolution of the reconstruction. Each cell of the host layer is reconstructed exactly (to machine precision) as 0. This exact result is probably due

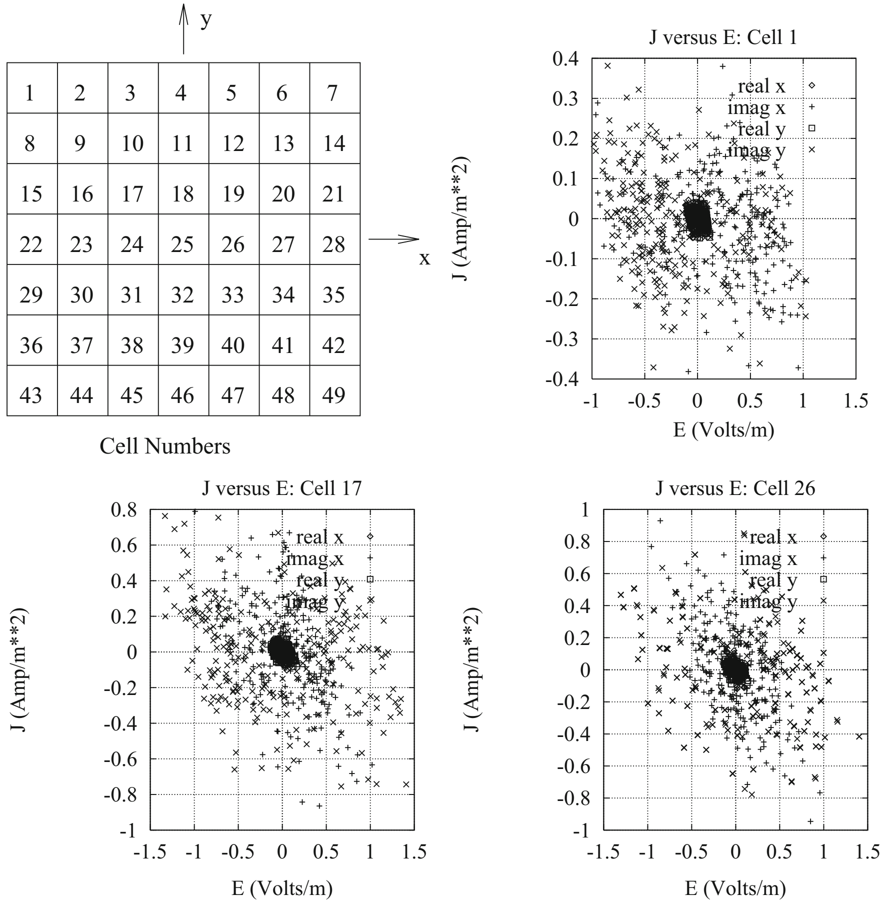

Fig. 2.5 Feasibility sets for the unflawed cells numbered 1, 17, and 26

to the fact that this part of the ‘flaw’ is uniform, which means that resolution is no problem. Furthermore, those parts of the flaw that are nearer the exciting source are generally reconstructed more accurately than those that are buried.

As for the buried part, it, too, is reconstructed well. We show in Fig. 2.9 several of the cells surrounding the slot that were not well reconstructed in Fig. 2.4; clearly, there is significant improvement in the reconstructions of these cells.

In performing this reconstruction we used the entire data set of 1024 points. If we use only the partial data sets associated with the real and imaginary parts of the x and y-components of the current density and electric field within each cell, we continued to get a good reconstruction, using either the S-estimator or the LMS-estimator. If we consider a performance criterion (or, perhaps we should say a parameter of confidence), to be the ratio of the largest value of the median (or estimate of scale in the case of the S-estimator) to the smallest, as θ (the conductivity

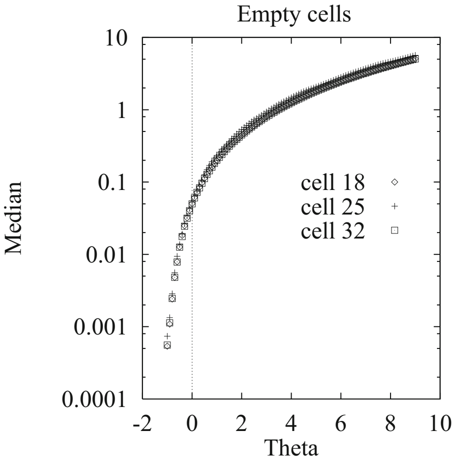

Fig. 2.6 Logarithm of the median-of-the-squares of the residual (LMS-algorithm) versus theta for cells 18, 25, 32

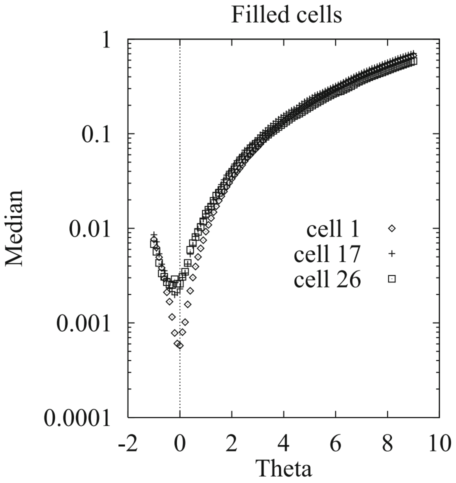

Fig. 2.7 Logarithm of the median-of-the-squares of the residual (LMS-algorithm) versus theta for cells 1, 17, and 26

slope) is varied from -1 to 0, then we found the use of the real and imaginary parts of the y-components to give, respectively, ratios of 100 and 200 for cell 73 (conductivity = -0.02 in Fig. 2.9). The use of the real and imaginary parts of the x-components gave, respectively, 40 and 180. When we used the entire data set of 1024 in cell 73, we computed a ratio of 105. In this sense, we can say that the imaginary part of both components provides superior data.

A Surface-Breaking Checkerboard at 50 MHz In this experiment we replace the simple slot of the first example by a complex checkerboard flaw that is shown in Fig. 2.10, and, again, perform a 16 × 16 raster scan with the transmitter and receiver probes at 50 MHz.

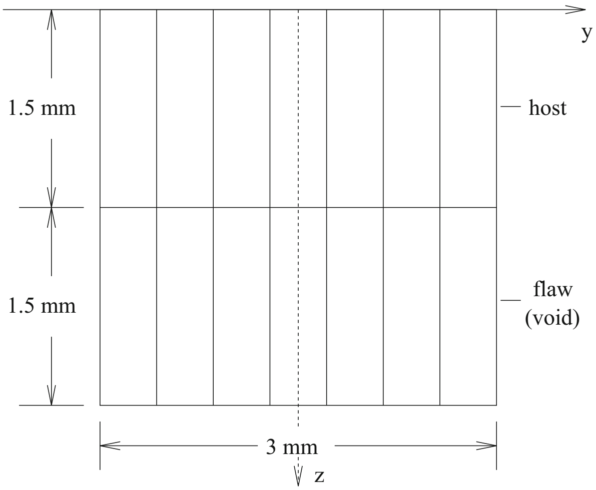

Fig. 2.8 A buried void. The upper grid corresponds to the 49 cells of the host layer, and the lower grid shows the flaw

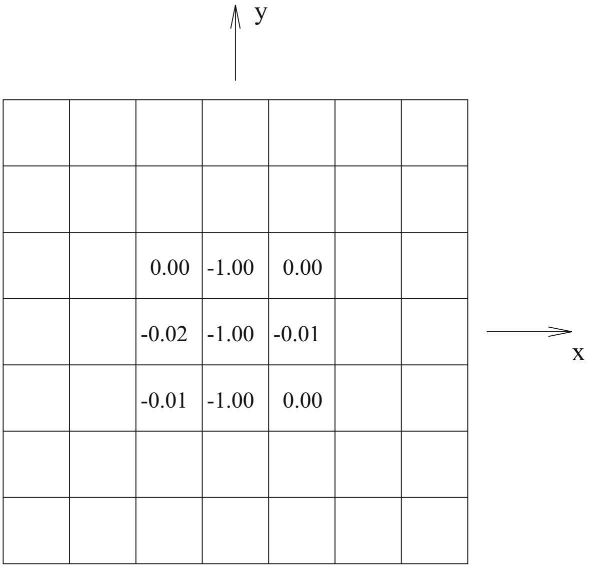

		0.00	-1.00	0.00		
		-0.02	-1.00	-0.01		
		-0.01	-1.00	0.00		

Fig. 2.9 Showing the reconstruction of several cells surrounding the slot, using the S-estimator. These are well reconstructed when compared to Fig. 2.4

The checkerboard is a difficult flaw to reconstruct, because the ‘scene’ changes so rapidly; i.e., it contains high spatial frequencies and the receiver scan must be fine enough to reconstruct these frequencies. The reconstruction using the LMS-estimator is quite good (corresponding results were obtained using the S-estimator and classical estimator). We show the reconstruction of the middle row and column in Fig. 2.11.

A Buried Checkerboard When we bury the checkerboard below a layer of host material we get the added complication of increasing the number of unknowns that

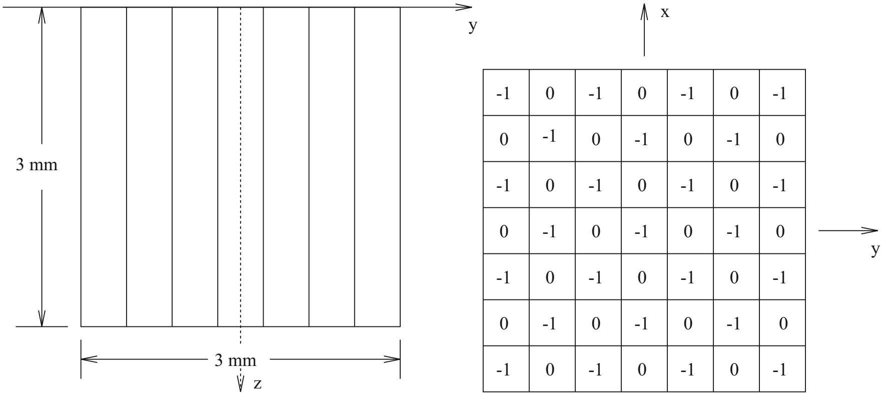

-1	0	-1	0	-1	0	-1
0	-1	0	-1	0	-1	0
-1	0	-1	0	-1	0	-1
0	-1	0	-1	0	-1	0
-1	0	-1	0	-1	0	-1
0	-1	0	-1	0	-1	0
-1	0	-1	0	-1	0	-1

Fig. 2.10 A surface-breaking checkerboard

Fig. 2.11 Reconstruction of the middle row and column of the surface-breaking checkerboard

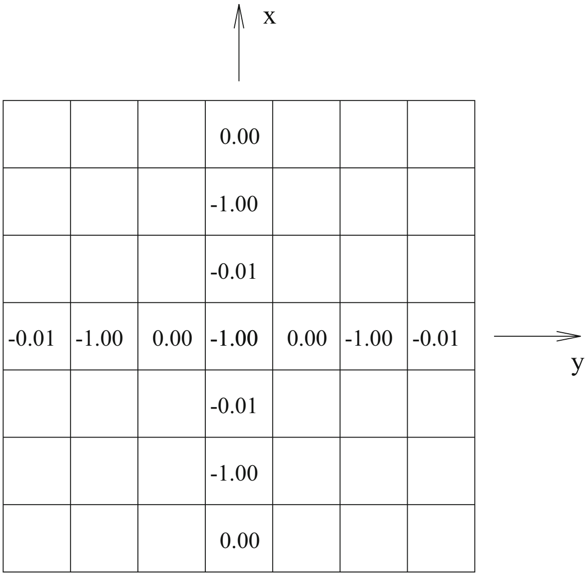

			0.00			
			-1.00			
			-0.01			
-0.01	-1.00	0.00	-1.00	0.00	-1.00	-0.01
			-0.01			
			-1.00			
			0.00			

are to be determined during the reconstruction. This, together with the fact that the checkerboard scene contains high spatial-frequencies, suggests that we use a 31×31 raster scan for the receiver probe, rather than the 16×16 scan that was used in the preceding examples, but covering the same area. The resolution of the receiver scan was thereby improved to 0.2 over 0.4 mm.

When we do this we get an excellent reconstruction; the top layer is reconstructed exactly (zero anomalous conductivity), and the reconstruction of the middle row and column of the bottom layer are shown in Fig. 2.12.

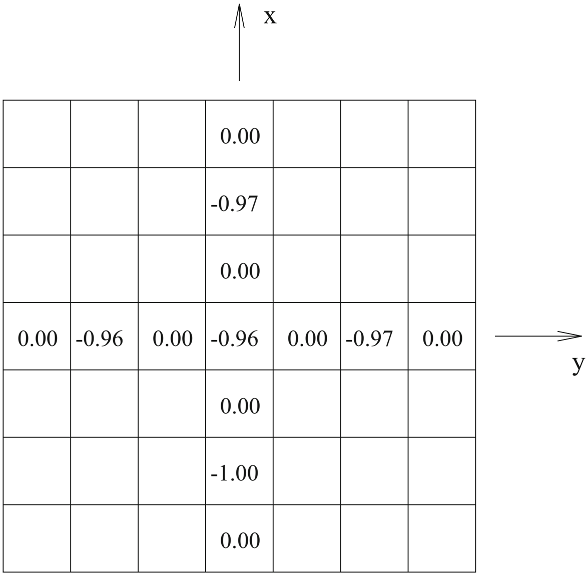

			0.00			
			-0.97			
			0.00			
0.00	-0.96	0.00	-0.96	0.00	-0.97	0.00
			0.00			
			-1.00			
			0.00			

Fig. 2.12 Reconstruction of the middle row and column of the buried checkerboard

When we attempted to reconstruct the buried checkerboard using the previous 16 × 16 raster scan with the receiver, we obtained a reasonable reconstruction– one that was good enough to indicate the presence of a checkerboard flaw beneath a layer of host material, but not as good as Fig. 2.12. See Fig. 2.13 for these results.

A Double Checkerboard When we stack two checkerboards with the opposite polarity on top of each other, and reconstruct at 50 MHz using a 31 × 31 receiver raster scan, we have difficulty obtaining an accurate reconstruction, except for the zeros of the top layer.

We have developed an empirical rule for determining the quality of a reconstructed cell, when using either the LMS or S-estimators. We plot the median of the squares of the residuals, in the case of the LMS-estimator, or the scale factor, in the case of the S-estimator, versus the sought-for parameter, θ, for $-1 \leq \theta \leq 9$ (say, or some other upper bound, perhaps 0). If the minimum value of the minimum median or scale factor is two or more orders of magnitude smaller than the maximum value of median or scale, then the resulting answer is reliable; otherwise, it is suspect. For example, in Fig. 2.14 we plot the curve of the logarithm of the median versus θ, for $-1 \leq \theta \leq 0$, for cell 1 (corner cell, top layer, conductivity = 0) and cell 2 (conductivity = -1). The curve for cell 1 clearly satisfies our empirical rule for a reliable reconstruction, whereas that for cell 2 does not. The reconstructed value for cell 1 is zero, whereas it is not well defined for cell 2.

The source of this problem in our inversion algorithm is the quantity and quality of data that are presented to the QR-decomposer in the first stage of the algorithm. Typically, the QR-method in least-squares analysis produces reliable results if the system of equations is quite over-determined. Hence, there are three possible ways

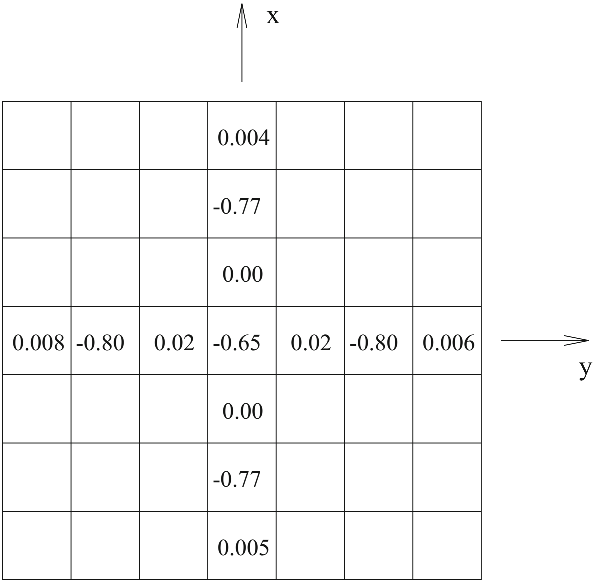

			0.004			
			-0.77			
			0.00			
0.008	-0.80	0.02	-0.65	0.02	-0.80	0.006
			0.00			
			-0.77			
			0.005			

Fig. 2.13 Reconstruction of a buried checkerboard, when a 16 × 16 receiver scan is used; the top layer was reconstructed perfectly. The classical (least-squares) estimator produced these results

Fig. 2.14 Log-median versus θ for cells 1 and 2

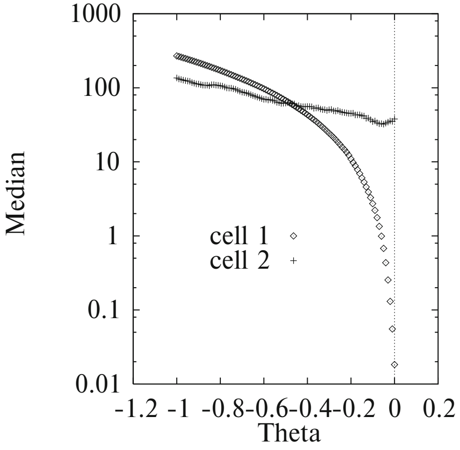

of improving the reconstruction of complex flaws of the double-checkerboard type: (1) increase the amount of input data by scanning the receiver probe over a larger range, with increased resolution, (2) using a different least-squares algorithm, such as Kaczmarz' [24, 27, 51] algorithm, that works well for even strongly underdetermined systems, or (3) modify our inversion algorithm to account for known constraints on certain correctly reconstructed cells.

2.6 Application to Aircraft Structures

The Canonical Problems The problems that will be solved in this section are:

1. Use **VIC-3D®** and our inversion algorithm to model the detection and characterization of metal corrosion in hidden or inaccessible airframe locations, such as double- or triple-layer airframes.
2. Use **VIC-3D®** and our inversion algorithm to model the detection and characterization of cracking or multisite damage in metallic airframe structures.
3. Use **VIC-3D®** and our inversion algorithm to model the detection, imaging, and characterization of surface and bulk anomalies in metallic airframe structures or engine components.

We can model corrosion as a weakly conducting region within a host material, and a crack as a nonconducting region within the same host. In fact, any region within the host material that is electrically distinct from the host will be called an anomalous region, and includes corrosion, cracks, fasteners, etc. We will take the host material to be aluminum, with a conductivity of 3.06×10^7 S/m, and a relative magnetic permeability of unity. In the problems that we will solve, we will replace 'corrosion' by a 'fastener,' whose conductivity is 16% that of aluminum. This is typical of brass, say.

The canonical structure for the inversion problems is shown in Fig. 2.15, which we will call a fastener with multisite damage. The structure consists of two layers, with the damage (or crack) emanating from opposite sides of the fastener in each layer.

Recall that the anomalous conductivity is given by $\sigma_f(\mathbf{r}) - \sigma_h$, where σ_f is the conductivity of the flaw, and σ_h the host conductivity. The normalized anomalous conductivity is simply the anomalous conductivity divided by the host conductivity. The conductivity of the crack will be zero, which means that the normalized anomalous conductivity of the crack will be -1. The normalized anomalous conductivity of the fastener is -0.84. Of course, the normalized anomalous conductivity of the host region is zero. Hence, the normalized anomalous conductivity-map of the structure is as shown in Fig. 2.16. We number the cells of the grid starting with the bottom layer, and working to the top. Cell number 1 is in the upper-left corner of the bottom layer, and cell number 64 is in the lower-right corner of the bottom layer. Cell number 65 is in the upper-left corner of the top layer (for a two-layer structure),

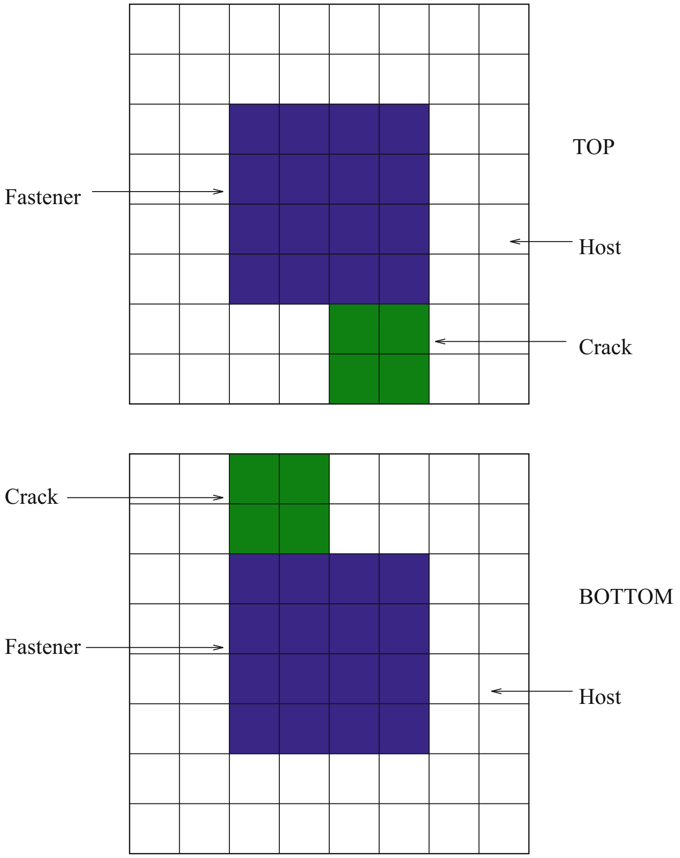

Fig. 2.15 Showing a fastener with multisite damage (the 'crack') embedded in a host region

and cell number 128 is in the lower-right corner. The length and width of the flaw will be 10 mm, and the depth 2.5 mm.

The data for the inversion experiments are gotten by assuming a transmit-receive system, in which the transmitter and receiver coils move independently of each other. The transmitter coil is taken to have an inner radius of 5 mm, an outer radius of 10 mm, a height of 2 mm, and to contain 200 turns. It undergoes a 4 × 4 raster scan in the (x, y) plane, which means that there are sixteen 'experiments,' in the language of set-theoretic estimation theory. The scan increment in the x- and y-directions is 3.3333 mm, which means that the raster scan covers the entire range of 10 × 10 square-millimeters of the flaw. The lift-off of the transmitter coil is 1 mm.

The receiver coil undergoes a 32 × 32 raster scan in the (x, y)-plane, again covering the 10 × 10 square-millimeters of the flaw. The inner radius of the receive coil is assumed to be 1 mm, the outer radius 2 mm, and the height 0.5 mm. The receive coil contains 200 turns, and its scan lift-off is zero.

0	0	0	0	0	0	0	0
0	0	0	0	0	0	0	0
0	0	-.84	-.84	-.84	-.84	0	0
0	0	-.84	-.84	-.84	-.84	0	0
0	0	-.84	-.84	-.84	-.84	0	0
0	0	-.84	-.84	-.84	-.84	0	0
0	0	0	0	-1.0	-1.0	0	0
0	0	0	0	-1.0	-1.0	0	0

TOP

0	0	-1.0	-1.0	0	0	0	0
0	0	-1.0	-1.0	0	0	0	0
0	0	-.84	-.84	-.84	-.84	0	0
0	0	-.84	-.84	-.84	-.84	0	0
0	0	-.84	-.84	-.84	-.84	0	0
0	0	-.84	-.84	-.84	-.84	0	0
0	0	0	0	0	0	0	0
0	0	0	0	0	0	0	0

BOTTOM

Fig. 2.16 Normalized anomalous conductivity-map of the fastener-with-multisite-damage structure

We have added noise to all the model impedance data used in our inversions. We assume that the noise has a zero-mean Gaussian distribution for both the magnitude and the phase of the impedance. We use a 1% variance in the magnitude and a 1° variance in the phase angle. These figures are realistic for contemporary instruments and data gathering techniques. As for the robust estimators, we have experimented with both, the Least Median of Squares (LMS) and the Scale (S) estimators, and

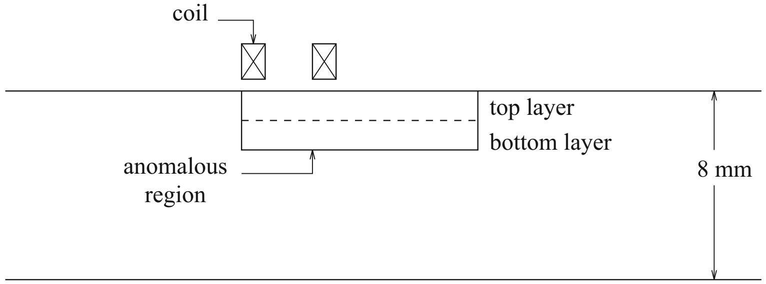

Fig. 2.17 Fastener with multisite damage as a surface-breaking anomaly

will report only the results of the S-estimator, which we call ‘stest’ in the captions of several figures.

Problem No. 1: Fastener with Multisite Damage in a Slab In the first problem, the anomalous region breaks the surface of a slab, as shown in Fig. 2.17. The data are gathered at 200 Hz.

The results for this problem are shown in Fig. 2.18.

Problem No. 2: Layer-Stripping Using Multifrequencies In an attempt to improve the results of Problem No. 1, we redo that problem by adopting a strategy, that we call layer-stripping using multifrequencies. The idea is to isolate the top layer of the anomalous region of Fig. 2.17 from the bottom layer. We do this by gathering data at a very high frequency, such that the incident field produced by the sensors does not penetrate to the bottom layer. This means that the anomalous currents in the cells of the bottom layer will not contribute to the measured impedances. Hence, we simply constrain these currents to be zero when we do the reconstruction starting with the QR-decomposition. We used **VIC-3D®** to determine suitable frequencies, trying 85, 170, and 340 kHz; we will report the results for 340 kHz.

The results of the inversion are shown in Fig. 2.19. The important point to note here is that the ‘zeroes’ in the upper layer are very sensitive to the systematic and random errors, and are therefore not well reconstructed, whereas the flaw and fastener cells are well reconstructed. This numerical experiment (and others which we will not report here) is the basis for determining a *heuristic rule*, which will be discussed now.

The stest-estimator generates a curve of scale, S, versus the normalized anomalous conductivity. The conductivity-estimate for each cell is chosen to be that which produces the (unique) minimum of this curve. In Fig. 2.20 we plot S versus conductivity for cells 86 and 87 of Fig. 2.19. Cell no. 86 contains flawed material, whereas no. 87 contains host material.

The minimum for cell no. 87 would, ideally, be sharply peaked at zero, but is quite broad, and lies too far to the left. Furthermore, it is a shallow null; i.e., the

-.06	-.16	-.26	-.24	-.12	-.08	+.02	-.02
-.10	-.14	-.18	-.18	-.16	-.08	-.02	-.04
-.22	-.22	-.75	-.88	-.80	-.72	-.12	-.08
-.30	-.40	-.72	-.74	-.72	-.76	-.36	-.26
-.20	-.42	-.72	-.76	-.74	-.74	-.52	-.48
-.10	-.12	-.70	-.78	-.72	-.72	-.40	-.34
-.08	-.02	-.08	-.18	-.68	-.72	-.38	-.26
-.02	0.0	-.06	-.16	-.82	-.88	-.04	+.02

TOP

-.06	-.08	-.16	-.26	-.18	-.16	-.08	-.02
-.10	-.12	-.22	-.30	-.22	-.18	-.10	-.06
-.14	-.16	-.36	-.42	-.42	-.32	-.16	-.10
-.16	-.16	-.40	-.56	-.60	-.34	-.18	-.12
-.14	-.16	-.38	-.60	-.60	-.48	-.18	-.14
-.10	-.14	-.32	-.36	-.50	-.40	-.18	-.12
-.04	-.06	-.18	-.26	-.36	-.30	-.18	-.18
+.04	0.0	-.10	-.18	-.32	-.24	-.08	0.0

BOTTOM

Fig. 2.18 Fastener with multisite damage. Reconstructed with 4 × 4 transmitter scan and 32 × 32 receiver scan, using the stest estimator. Noise: 1% relative magnitude error; 1° phase error

ratio of the largest to the smallest value of S is not large, typically five or less. On the other hand, the minimum for cell no. 86 *is* quite sharply peaked at a value of -0.86, which is quite close to its ‘correct’ value of -0.84. Furthermore, the minimum is much deeper than that for cell no. 87. This, then, is the basis of our **heuristic rule: if host cells and anomalous cells occupy the same layer, the host cells are quite poorly resolved compared to the anomalous cells. Hence, when we see curves such as those in Fig. 2.20, we will assume that cells, such as no. 87, for which**

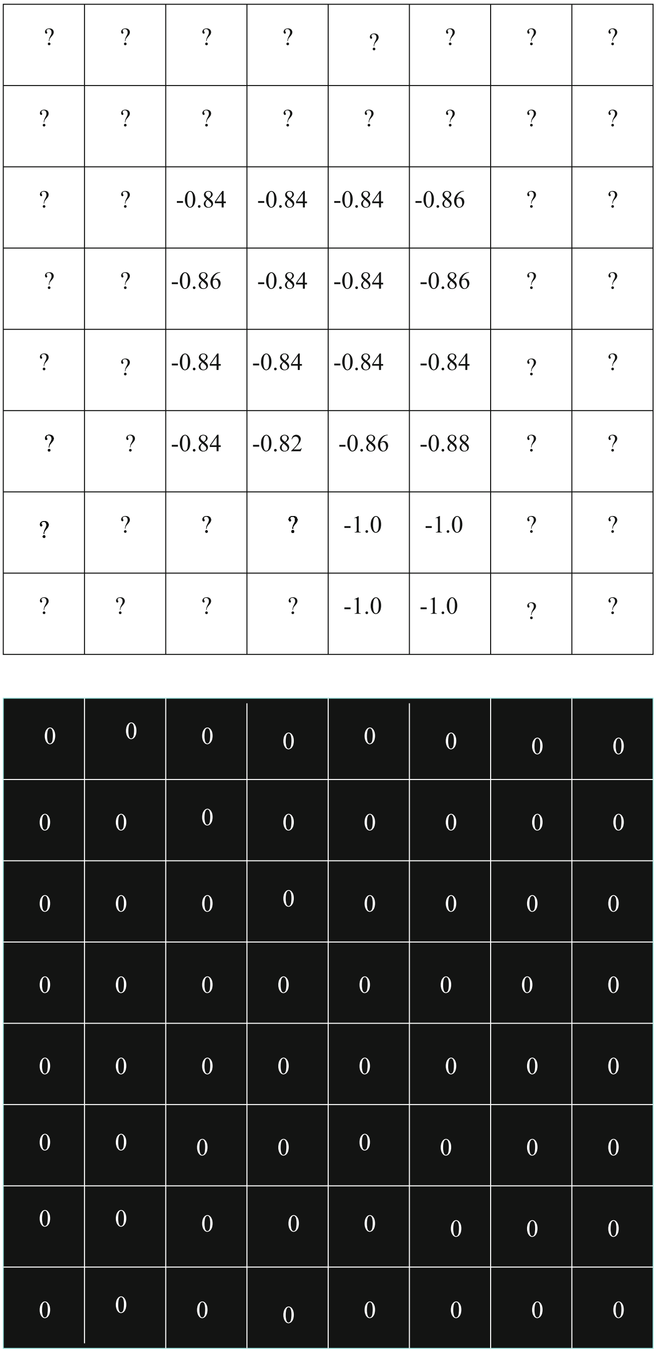

?	?	?	?	?	?	?	?
?	?	?	?	?	?	?	?
?	?	-0.84	-0.84	-0.84	-0.86	?	?
?	?	-0.86	-0.84	-0.84	-0.86	?	?
?	?	-0.84	-0.84	-0.84	-0.84	?	?
?	?	-0.84	-0.82	-0.86	-0.88	?	?
?	?	?	?	-1.0	-1.0	?	?
?	?	?	?	-1.0	-1.0	?	?

0	0	0	0	0	0	0	0
0	0	0	0	0	0	0	0
0	0	0	0	0	0	0	0
0	0	0	0	0	0	0	0
0	0	0	0	0	0	0	0
0	0	0	0	0	0	0	0
0	0	0	0	0	0	0	0
0	0	0	0	0	0	0	0

Fig. 2.19 Fastener with multisite damage. Reconstructed with 4 × 4 transmitter scan and 32 × 32 receiver scan. This is an example of layer-stripping with multifrequencies, using the stest estimator. Noise: 1% relative magnitude error; 1° phase error. Cells of the top layer, that are marked with a '?', have poorly resolved zeroes. Cells of the bottom layer, marked with a zero and shown in black, are forced to have a zero conductivity

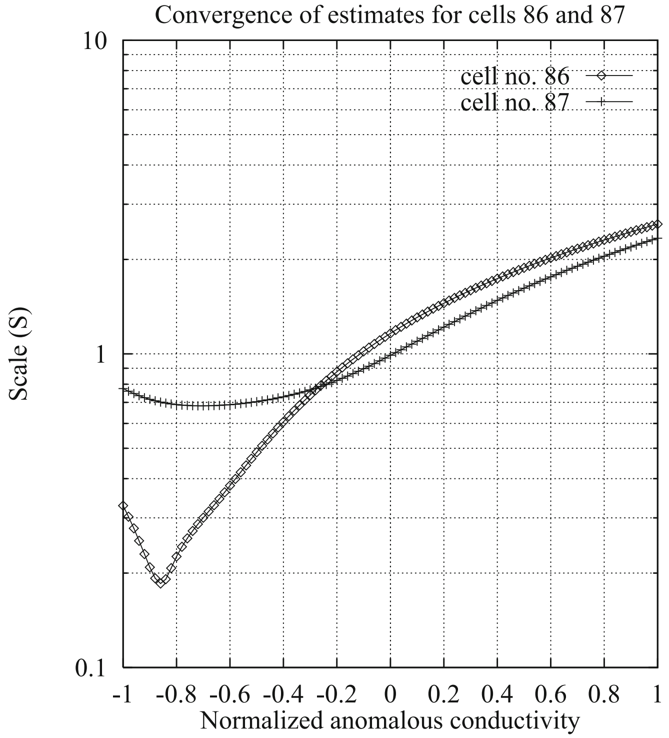

Fig. 2.20 Scale, S, versus normalized anomalous conductivity for cells 86 and 87 of Fig. 2.19. Cell no. 86 contains flawed material, whereas no. 87 contains host material

the ratio of the largest to the smallest value of S is five (5) or less, should have a zero value for the normalized anomalous conductivity.

When we apply the heuristic rule, and force the appropriate cells in the upper layer to have zero anomalous conductivity, we obtain the improved results of Fig. 2.21. Note that by a rather straightforward post-processing algorithm, we have virtually eliminated the effects of noise.

Furthermore, we have even improved the solution for cell no. 86, as we see in Fig. 2.22. Here we plot S vs. conductivity for cell no. 86, when the conditions of Figs. 2.19 (unforced zeros) and 2.21 (forced zeros) hold. Note that the curve is even more sharply peaked downward when the appropriate cells of the top layer are forced to be zero than when they are not. Furthermore, the new estimate of the value of the normalized anomalous conductivity *is* now -0.84, which agrees with the original model.

At this point, the logic of the layer-stripping algorithm would have us use the results for the top layer as a constraint when reconstructing the bottom layer at a lower frequency, say 200 Hz. This is why the algorithm is called a multifrequency layer-stripping algorithm. We cannot proceed to do this, however, because the

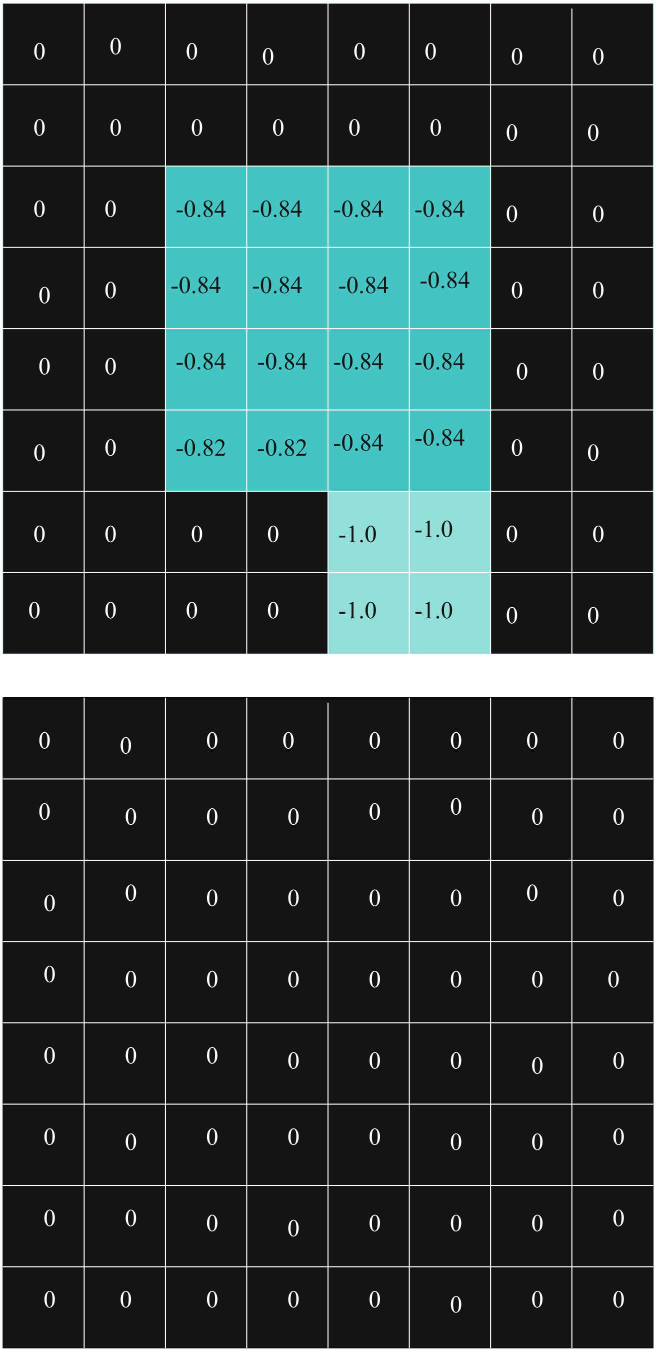

0	0	0	0	0	0	0	0
0	0	0	0	0	0	0	0
0	0	-0.84	-0.84	-0.84	-0.84	0	0
0	0	-0.84	-0.84	-0.84	-0.84	0	0
0	0	-0.84	-0.84	-0.84	-0.84	0	0
0	0	-0.82	-0.82	-0.84	-0.84	0	0
0	0	0	0	-1.0	-1.0	0	0
0	0	0	0	-1.0	-1.0	0	0

0	0	0	0	0	0	0	0
0	0	0	0	0	0	0	0
0	0	0	0	0	0	0	0
0	0	0	0	0	0	0	0
0	0	0	0	0	0	0	0
0	0	0	0	0	0	0	0
0	0	0	0	0	0	0	0
0	0	0	0	0	0	0	0

Fig. 2.21 Results for the same system as Fig. 2.19, except that the appropriate cells in the upper layer are forced to have zero anomalous conductivity. Hence, all cells labeled '0', which are shown in black, have been forced to have zero anomalous conductivity

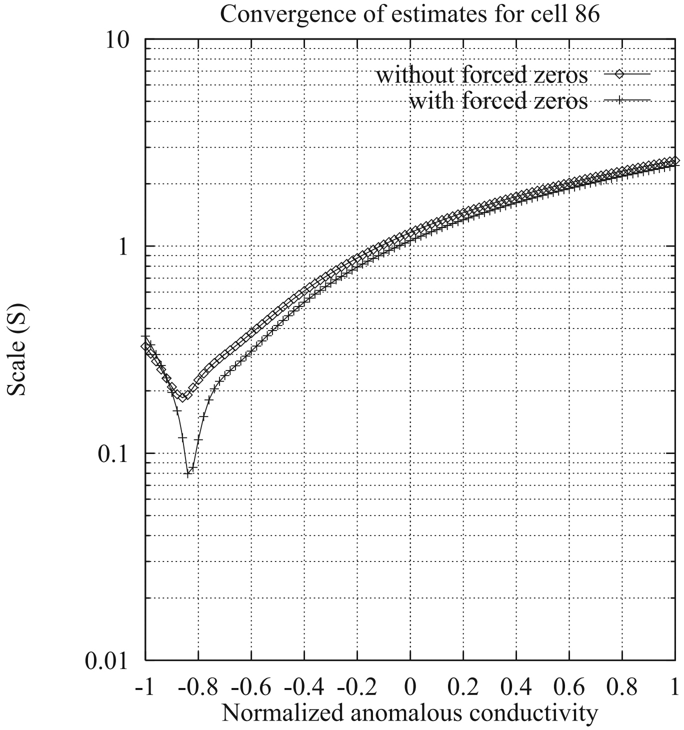

Fig. 2.22 Scale, S, versus normalized anomalous conductivity for cell no. 86 before (diamond) and after (+) forcing zeros for the appropriate cells in the upper layer

current version of **VIC-3D®** allows us only to apply constraints when a cell has a zero anomalous conductivity.

Problem No. 3: Fastener with Multisite Damage in Bottom Plate of a Double-Plate System In this problem, we take the same anomaly as before (the fastener with multisite damage) and put in the bottom plate of a double-plate system, as shown in Fig. 2.23. Each plate is 2.5 mm thick, and the distance between them is 1 mm. The anomaly, therefore, penetrates the bottom layer (a 'throughwall' anomaly).

In order to make the problem more interesting, we consider the anomaly to lie in four layers, rather than two. The bottom two layers repeat the bottom layer of Fig. 2.15, and the top two layers repeat the top layer of that figure. The numerical experiment is run at 200 Hz, and the results shown in Fig. 2.24. As before, the '?' denotes a poorly resolved cell, which, according to our heuristic rule, will be interpreted as being a cell containing host material, so that its conductivity will be constrained to be zero.

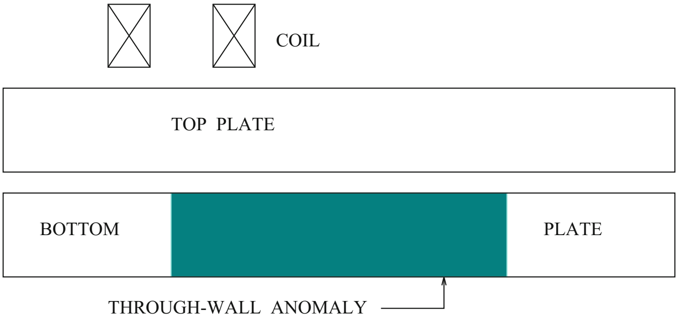

Fig. 2.23 Fastener with multisite damage in bottom plate of a double-plate system

2

?	?	-.24	-.38	?	?	?	?
?	?	-.33	-.42	?	?	?	?
?	?	-.46	-.58	-.55	-.44	?	?
?	?	-.55	-.64	-.64	-.54	?	?
?	?	-.53	-.64	-.64	-.54	?	?
?	?	-.44	-.56	-.60	-.52	?	?
?	?	?	?	?	?	?	?
?	?	?	?	?	?	?	?

4

?	?	?	?	?	?	?	?
?	?	?	?	?	?	?	?
?	?	-.64	-.80	-.81	-.57	?	?
?	?	-.84	-1.0	-1.0	-.78	?	?
?	?	-.77	-.91	-.92	-.74	?	?
?	?	-.51	-.69	-.85	-.72	?	?
?	?	?	?	-.87	-.78	?	?
?	?	?	?	-.56	-.52	?	?

1

?	?	-.26	-.40	?	?	?	?
?	?	-.32	-.41	?	?	?	?
?	?	-.41	-.49	-.48	-.38	?	?
?	?	-.48	-.54	-.56	-.46	?	?
?	?	-.46	-.56	-.58	-.48	?	?
?	?	-.38	-.48	-.52	-.45	?	?
?	?	?	?	?	?	?	?
?	?	?	?	?	?	?	?

3

?	?	?	?	?	?	?	?
?	?	?	?	?	?	?	?
?	?	-.54	-.65	-.65	-.49	?	?
?	?	-.65	-.82	-.80	-.64	?	?
?	?	-.63	-.76	-.76	-.62	?	?
?	?	-.48	-.62	-.72	-.62	?	?
?	?	?	?	-.61	-.58	?	?
?	?	?	?	-.41	-.38	?	?

Fig. 2.24 Fastener with multisite damage in second plate of double-plate system. Reconstructed with 4 × 4 transmitter scan and 32 × 32 receiver scan, using the stest estimator. Noise: 1% relative magnitude error; 1° phase error. The layers are numbered from bottom to top

4

0	0	0	0	0	0	0	0
0	0	0	0	0	0	0	0
0	0	-.15	-.85	-.82	-.28	0	0
0	0	-.86	-1.0	-1.0	-.74	0	0
0	0	-.80	-.84	-.87	-.72	0	0
0	0	-.24	-.57	-.84	-.78	0	0
0	0	0	0	-.94	-.78	0	0
0	0	0	0	-.57	-.52	0	0

These zeros are forced

Fig. 2.25 Results for the fourth (top) layer of Fig. 2.24, when cells in only the fourth layer are constrained

When we force the appropriate cells of only the fourth (top) layer to be zero, we get the results shown in Fig. 2.25 for the fourth layer. There is a significant improvement compared to Fig. 2.24.

If, however, we constrain the appropriate cells in all of the layers, then we get the dramatic improvement shown in Fig. 2.26.

Even though the results are excellent, there remains an interesting anomaly in them. Note the twelve circled cells; their conductivities are too low. This is a manifestation of the failure of the 'two-cell hypothesis,' because two of the four nearest neighbor cells have perfect zero anomalous conductivities. Hence, the hypothesis must fail in 50% of the cases for these cells. Nevertheless, this anomaly is easily recognized, and easily cured. We simply redo the two-cell hypothesis using the two nearest neighbors that have nonzero conductivities, and recalculate the conductivities using the robust estimator. When we do this we get excellent agreement with the true value for these cells.

Problem No. 4: Another Layer-Stripping Example Using Multifrequencies This problem concerns a buried flaw in an aluminum slab. The anomalous region is again modeled as a two-layer system, as in Fig. 2.17, but the top layer is simply host material (anomalous conductivity of zero for each cell). The bottom layer is identical to the bottom layer of Fig. 2.15.

Because we do not know a priori that the top layer is host material, we run the problem first at 85 kHz, in order to reconstruct the top layer independently of the bottom, as in Problem No. 2. This is done by forcing the bottom cells to have zero anomalous conductivity, as in Fig. 2.27.

The reconstruction of the top layer produces excellent zeros for all of the cells, as we would hope. This is not a violation of the heuristic rule that was defined in

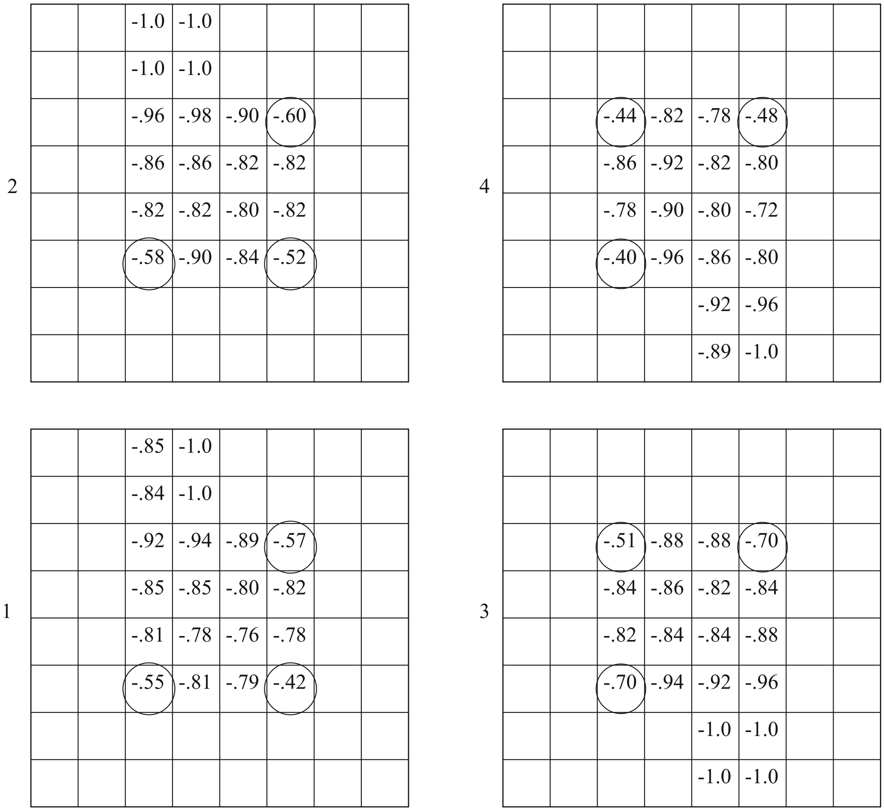

2

		-1.0	-1.0				
		-1.0	-1.0				
		-.96	-.98	-.90	-.60		
		-.86	-.86	-.82	-.82		
		-.82	-.82	-.80	-.82		
		-.58	-.90	-.84	-.52		

4

		-.44	-.82	-.78	-.48		
		-.86	-.92	-.82	-.80		
		-.78	-.90	-.80	-.72		
		-.40	-.96	-.86	-.80		
				-.92	-.96		
				-.89	-1.0		

1

		-.85	-1.0				
		-.84	-1.0				
		-.92	-.94	-.89	-.57		
		-.85	-.85	-.80	-.82		
		-.81	-.78	-.76	-.78		
		-.55	-.81	-.79	-.42		

3

		-.51	-.88	-.88	-.70		
		-.84	-.86	-.82	-.84		
		-.82	-.84	-.84	-.88		
		-.70	-.94	-.92	-.96		
				-1.0	-1.0		
				-1.0	-1.0		

Fig. 2.26 Results for all four layers of Fig. 2.24 when the appropriate cells (which are unmarked in this figure) in all four layers are constrained to have zero relative anomalous conductivity. The twelve circled cells have values that are too low because of the failure of the 'two-cell hypothesis.'

Problem No. 2, because there are only host cells in the top layer, not a mixture of host and anomalous cells.

Next, we rerun the problem at 200 Hz, constraining the top cells to have zero conductivity, because that is what the reconstruction produced. This is the 'layer-stripping' step, and we can rigorously apply it in this example because the layer stripped-off has only zero-conductivity cells. The result is shown in Fig. 2.28.

When we apply the heuristic rule to the bottom layer of Fig. 2.28, and force the appropriate cells to take the value of zero, we get the excellent reconstruction shown in Fig. 2.29. The cells shown in black are forced to have zero conductivity. The anomalously low values of three cells are due to the 'two-cell' hypothesis, and can be corrected as described before.

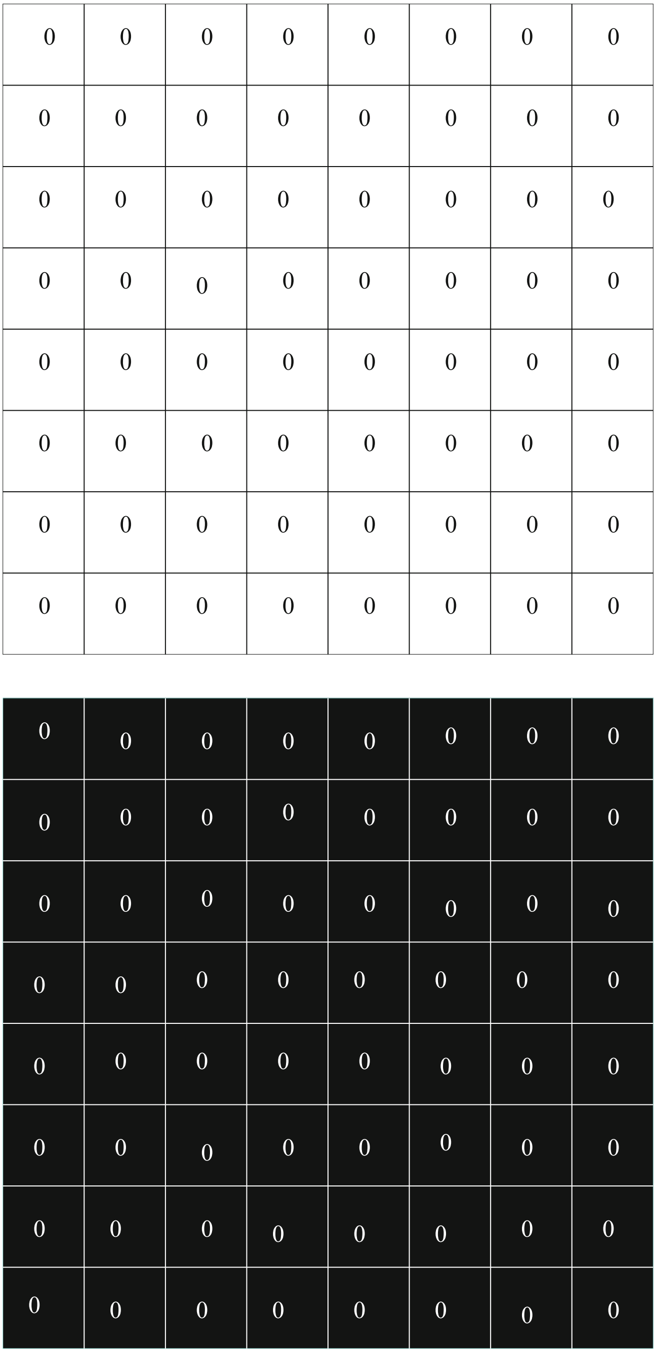

0	0	0	0	0	0	0	0
0	0	0	0	0	0	0	0
0	0	0	0	0	0	0	0
0	0	0	0	0	0	0	0
0	0	0	0	0	0	0	0
0	0	0	0	0	0	0	0
0	0	0	0	0	0	0	0
0	0	0	0	0	0	0	0

0	0	0	0	0	0	0	0
0	0	0	0	0	0	0	0
0	0	0	0	0	0	0	0
0	0	0	0	0	0	0	0
0	0	0	0	0	0	0	0
0	0	0	0	0	0	0	0
0	0	0	0	0	0	0	0
0	0	0	0	0	0	0	0

Fig. 2.27 Reconstruction at 85 kHz, with the bottom layer constrained to have zero anomalous conductivity in each cell (shown in black). The cells of the top layer are freely reconstructed in accordance with the inversion algorithm, and produce very well-resolved zeros

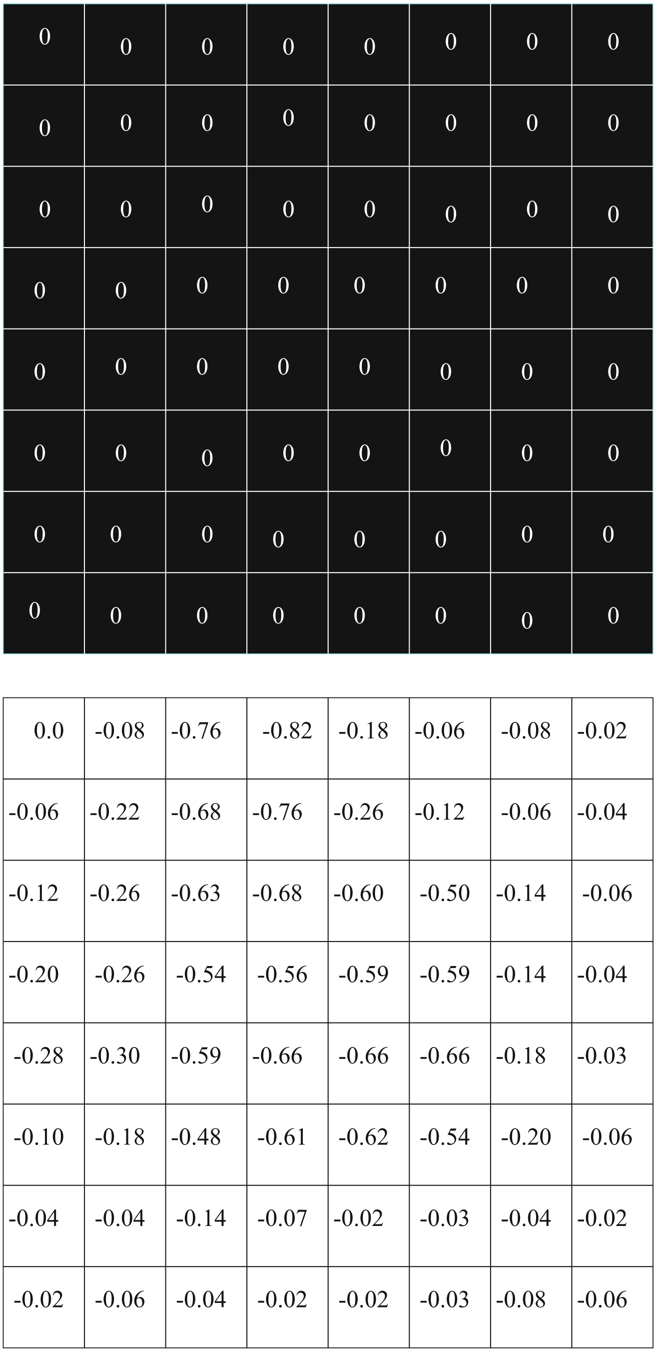

0	0	0	0	0	0	0	0
0	0	0	0	0	0	0	0
0	0	0	0	0	0	0	0
0	0	0	0	0	0	0	0
0	0	0	0	0	0	0	0
0	0	0	0	0	0	0	0
0	0	0	0	0	0	0	0
0	0	0	0	0	0	0	0

0.0	-0.08	-0.76	-0.82	-0.18	-0.06	-0.08	-0.02
-0.06	-0.22	-0.68	-0.76	-0.26	-0.12	-0.06	-0.04
-0.12	-0.26	-0.63	-0.68	-0.60	-0.50	-0.14	-0.06
-0.20	-0.26	-0.54	-0.56	-0.59	-0.59	-0.14	-0.04
-0.28	-0.30	-0.59	-0.66	-0.66	-0.66	-0.18	-0.03
-0.10	-0.18	-0.48	-0.61	-0.62	-0.54	-0.20	-0.06
-0.04	-0.04	-0.14	-0.07	-0.02	-0.03	-0.04	-0.02
-0.02	-0.06	-0.04	-0.02	-0.02	-0.03	-0.08	-0.06

Fig. 2.28 Reconstruction of buried flaw, using layer-stripping. Only the cells of the top layer (shown in black) have been forced to have zero conductivity. The frequency is 200 Hz

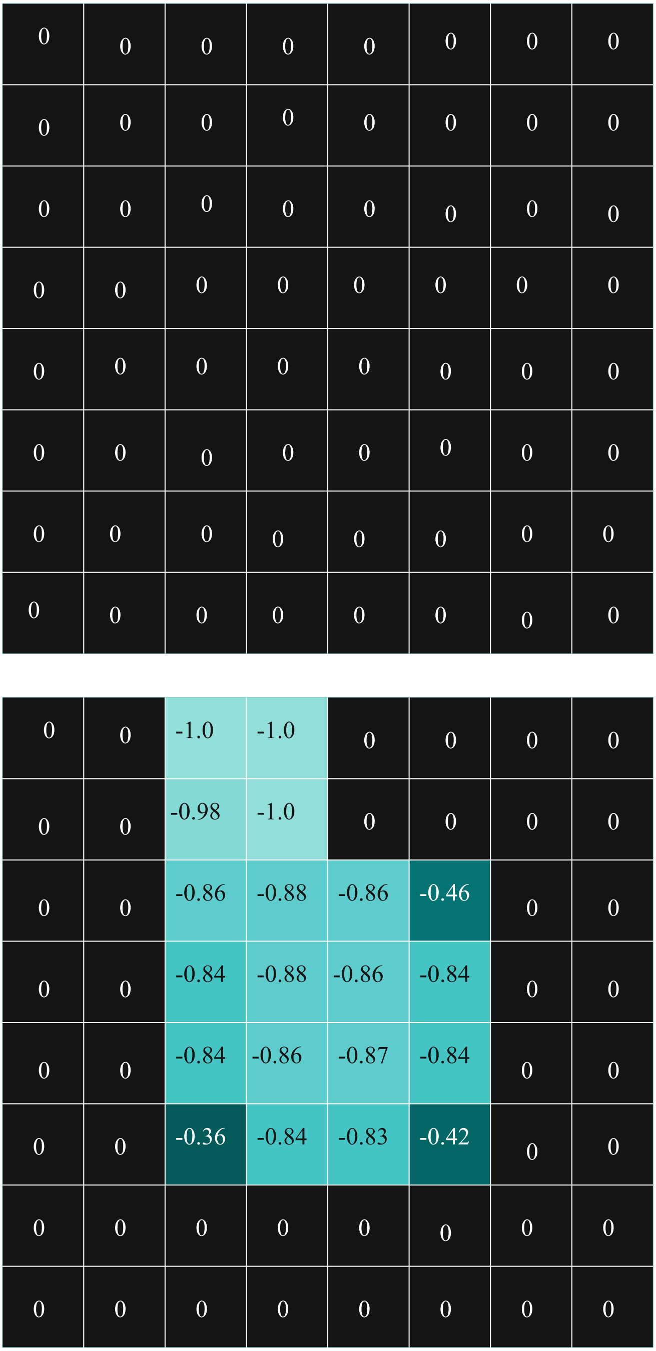

0	0	0	0	0	0	0	0
0	0	0	0	0	0	0	0
0	0	0	0	0	0	0	0
0	0	0	0	0	0	0	0
0	0	0	0	0	0	0	0
0	0	0	0	0	0	0	0
0	0	0	0	0	0	0	0
0	0	0	0	0	0	0	0

0	0	-1.0	-1.0	0	0	0	0
0	0	-0.98	-1.0	0	0	0	0
0	0	-0.86	-0.88	-0.86	-0.46	0	0
0	0	-0.84	-0.88	-0.86	-0.84	0	0
0	0	-0.84	-0.86	-0.87	-0.84	0	0
0	0	-0.36	-0.84	-0.83	-0.42	0	0
0	0	0	0	0	0	0	0
0	0	0	0	0	0	0	0

Fig. 2.29 Reconstruction of buried flaw, using layer-stripping. All of the cells labeled zero, and shown in black, have been forced to have zero anomalous conductivity. The color map in the bottom figure has a resolution of only 5%